Monthly Notices
of the
ROYAL ASTRONOMICAL SOCIETY

MNRAS **494,** 2355–2373 (2020)
Advance Access publication 2020 April 7

doi:10.1093/mnras/staa848

The influence of a top-heavy integrated galactic IMF and dust on the chemical evolution of high-redshift starbursts

M. Palla [1,2★] F. Calura [3★] F. Matteucci,[1,4,5] X. L. Fan [6] F. Vincenzo [7] and E. Lacchin[1,3,8]

[1]*Dipartimento di Fisica, Sezione di Astronomia, Universitá degli Studi di Trieste, via G. B. Tiepolo 11, I-34131 Trieste, Italy*
[2]*IFPU - Institute for Fundamental Physics of the Universe, Via Beirut 2, I-34014 Trieste, Italy*
[3]*INAF - OAS, Osservatorio di Astrofisica e Scienza dello Spazio di Bologna, via Gobetti 93/3, I-40129 Bologna, Italy*
[4]*INAF, Osservatorio Astronomico di Trieste, via G. B. Tiepolo 11, I-34131 Trieste, Italy*
[5]*INFN, Sezione di Trieste, via A. Valerio 2, I-34100 Trieste, Italy*
[6]*School of Physics and Technology, Wuhan University, 430072, Wuhan, Hubei 430205, China*
[7]*Center for Cosmology and AstroParticle Physics, The Ohio State University, 191 West Woodruff Avenue, Columbus, OH 43210, USA*
[8]*Dipartimento di Fisica e Astronomia, Universitá di Bologna, via Gobetti 93/2, I-40129 Bologna, Italy*

Accepted 2020 March 24. Received 2020 March 24; in original form 2020 March 4

ABSTRACT

We study the effects of the integrated galactic initial mass function (IGIMF) and dust evolution on the abundance patterns of high redshift starburst galaxies. In our chemical models, the rapid collapse of gas clouds triggers an intense and rapid star formation episode, which lasts until the onset of a galactic wind, powered by the thermal energy injected by stellar winds and supernova explosions. Our models follow the evolution of several chemical elements (C, N, α-elements, and Fe) both in the gas and dust phases. We test different values of β, the slope of the embedded cluster mass function for the IGIMF, where lower β values imply a more top-heavy initial mass function (IMF). The computed abundances are compared to high-quality abundance measurements obtained in lensed galaxies and from composite spectra in large samples of star-forming galaxies in the redshift range $2 \lesssim z \lesssim 3$. The adoption of the IGIMF causes a sensible increase of the rate of star formation with respect to a standard Salpeter IMF, with a strong impact on chemical evolution. We find that in order to reproduce the observed abundance patterns in these galaxies, either we need a very top-heavy IGIMF ($\beta < 2$) or large amounts of dust. In particular, if dust is important, the IGIMF should have $\beta \geq 2$, which means an IMF slightly more top-heavy than the Salpeter one. The evolution of the dust mass with time for galaxies of different mass and IMF is also computed, highlighting that the dust amount increases with a top-heavier IGIMF.

Key words: stars: luminosity function, mass function – dust, extinction – galaxies: abundances – galaxies: evolution – galaxies: starburst .

1 INTRODUCTION

The stellar initial mass function (IMF) influences most observable properties of stellar populations, as it regulates the relative fractions of low- and high-mass stars within them.

Massive stars (i.e. the stars with mass $>8\,M_{\odot}$) are known to be the main producers of α-elements[1] over short ($\leq$30 Myr) time-scales. On the other hand, the bulk of Fe in a galaxy is known to be produced by Type Ia supernovae (SNe) over time-scales that can even reach or exceed the Hubble time (Matteucci & Greggio 1986; Matteucci & Recchi 2001). Owing to these differences, chemical abundance ratios have been used as powerful instruments for reconstructing the star formation history of galaxies.

Besides chemical evolution, many other properties of a galaxy are strictly related to the IMF, such as the present time stellar mass (Kennicutt 1998), the integrated light of galaxies (Conroy & van Dokkum 2012b) as well as energetic feedback from massive stars. At present, a complete theory able to explain the origin of the IMF does not exist. Another fundamental issue yet to be clarified concerns the universality of the IMF, as in principle in the local Universe it could be different from high redshift galaxies (e.g.

★ E-mail: marco.ball94@gmail.com (MP); francesco.calura@inaf.it (FC)

[1]Elements characterized by capture of α particles. Examples are O, Mg, Si, S, Ca.

Larson 1998), which are likely to be characterized by different physical conditions.

In this framework, a significant role is played by the integrated galactic initial mass function (IGIMF) theory (e. g., Kroupa & Weidner 2003; Weidner & Kroupa 2005). It is based on a few basic empirical evidences related to the birth of stars in local star-forming environments, which include the fact that: (i) stars form in a clustered mode (Lada & Lada 2003; Megeath et al. 2016), i.e. in groups of at least a few stars in the dense molecular cloud cores; (ii) within each stellar cluster, the IMF is observed to be universal and well approximated by a multiple power-law form (Massey & Hunter 1998; Pflamm-Altenburg, Weidner & Kroupa 2007); (iii) stellar clusters are distributed according to a single-slope power law (Lada & Lada 2003) and (iv) the upper mass end of the embedded cluster mass function has been found to depend on the star formation rate (SFR) of the galaxy (Weidner & Kroupa 2004). The main consequence of these evidences is that the integrated IMF in disc galaxies (such as the Milky Way) is generally steeper than the stellar IMF within each single star cluster (Kroupa & Weidner 2003).

Weidner, Kroupa & Pflamm-Altenburg (2011) extended the IGIMF theory to systems characterized by high star formation rates (SFR $> 10\,\mathrm{M}_{\odot}\,\mathrm{yr}^{-1}$), showing that in the most intensely star-forming objects, i.e. in very massive and compact systems, the resulting IMF becomes top-heavy, with extreme consequences on chemical enrichment and on stellar feedback.

Various other studies indicated that a high-redshift top-heavy IMF seems to be required to explain several properties of massive galaxies. These properties include the observed evolution of the optical luminosity density (Larson 1998), the integrated [α/Fe] ratios (Calura & Menci 2009; De Masi, Matteucci & Vincenzo 2018) and the colour-luminosity relation (Gibson & Matteucci 1997) in local spheroids, the observed galaxy number counts in the infrared band and at submillimetric wavelengths (Baugh et al. 2005), the isotopic ratios in high-z starbursts (Romano et al. 2017; Zhang et al. 2018) and the discrepancy between the observed present-day stellar mass density and the integral of the comoving SFR density (Davé 2008). In order to conciliate other indications in early-type galaxies (e.g. Cenarro et al. 2003; Conroy & van Dokkum 2012a,b; La Barbera et al. 2013) suggesting a bottom-heavy IMF, Weidner et al. (2013) and Ferreras et al. (2015) proposed also a time-dependent form of the IMF, switching from top-heavy during the initial burst of star formation to bottom-heavy at later times.

Several evidences support the idea that local spheroids must have experienced a starburst phase at high redshift. This is inferred from the record of their stellar populations, in particular from their integrated ages and integrated abundances (e.g. Matteucci 1994; Spolaor et al. 2010 and references therein). In principle, high-redshift starbursts might also present the physical conditions required for a top-heavy IMF, whose signature might be encoded in their interstellar abundance pattern. For this reason, the turbulent, strongly pressurized ISM of starbursts represents an ideal laboratory to probe the IMF in the progenitors of local spheroids, and in particular to test the hypothesis of a top-heavy IMF during the starburst phase.

The investigation of the physical conditions of high-redshift starbursts as traced by their observed abundance pattern is the main motivation of this paper. By means of chemical evolution models for protospheroids, for the first time we aim at testing the effects of a top-heavy IGIMF on the chemical evolution of starbursts. The results of our models will be compared with high-quality data from lensed high-redshift starbursts. Our models allow us to follow the evolution of the chemical abundances of several species (C, N, α-elements, and Fe), both in the gas and in the dust phases. In fact, our models can account for differential dust depletion that allows us to study the abundances of refractory elements (e.g. Mg, Fe) in such objects. It is worth noting that this paper is the first in which a detailed treatment of dust is included in chemical evolution models with the IGIMF. The inclusion of dust will be particularly insightful, as previous chemical evolution models which did not take into account this ingredient failed to reproduce the [α/Fe] ratios observed in similar objects, such as Lyman Break galaxies (LBGs; Matteucci & Pipino 2002; Pipino et al. 2011).

This work follows various studies carried on in the last few years, aimed at assessing the effects of the IGIMF on galactic chemical evolution in various environments characterized by different star formation histories, i.e. the solar neighbourhood (Calura et al. 2010), dwarf galaxies (Vincenzo et al. 2015, Lacchin et al. 2019), and local elliptical galaxies (Recchi, Calura & Kroupa 2009; De Masi et al. 2018).

A novel formulation of the IGIMF was recently proposed by Yan, Jerabkova & Kroupa (2017) and Jeřábková et al. (2017, 2018) and firstly tested by Yan et al. (2019) for elliptical galaxies. The implementation of such new formulation in models for starburst galaxies might be the subject of a future work.

The paper is organized as follows: in Section 2, we describe the IGIMF theory and chemical and dust evolution models adopted in this work. Our observational data are described in Section 3. Our results are presented in Section 4. Finally, conclusions are drawn in Section 5.

2 MODELS

In this Section, we will describe the IGIMF theory and the main features of the chemical evolution models adopted in this paper. We will describe the basic physical ingredients of the models, which are aimed at describing the starburst phase of massive protospheroids. Finally, we will outline the main assumptions regarding the main processes regulating dust evolution, which also have a strong influence on interstellar abundances.

2.1 IGIMF

Following the works of Kroupa & Weidner (2003) and Weidner & Kroupa (2005), the IGIMF is defined by weighting the canonical IMF, $\phi(m)$ (described later in this Section), with the mass distribution of the stellar clusters (called embedded cluster mass function, ECMF), $\xi_{\rm ecl}(M_{\rm ecl})$. The IGIMF theory starts from the assumption that star formation takes place in molecular cloud cores, i.e. in embedded stellar clusters. The IGIMF $\xi_{\rm IGIMF}(m,t)$ can be expressed as a function of stellar mass m and time t as:

$$\xi_{\rm IGIMF}(m,t) = \int_{M_{\rm ecl,min}}^{M_{\rm ecl,max}(\psi(t))} \phi(m \leq m_{\rm max}(M_{\rm ecl}))\,\xi_{\rm ecl}(M_{\rm ecl})\,{\rm d}M_{\rm ecl}, \quad (1)$$

where $M_{\rm ecl}$ is the cluster mass.

The IGIMF is normalized as

$$\int_{m_{min}}^{m_{max}} m\,\xi_{\rm IGIMF}(m,t)\,{\rm d}m = 1.$$

As can be seen from equation (1), the IGIMF adopted in this work has a time dependence, which is due to the SFR $\psi(t)$ of the parent galaxy, following the model of Weidner et al. (2011) (hereafter

W11). In the following, we will list the assumptions, based on empirical evidence, on which the IGIMF theory is based.

(i) The ECMF is represented by a single-slope power law:

$$\xi_{\rm ecl}(M_{\rm ecl}) \propto \left(\frac{M_{\rm ecl}}{M_{\rm ecl,max}}\right)^{-\beta}, \quad (2)$$

where the slope β can vary between $\beta = 0.5$ and $\beta = 2.35$.
The adopted minimum cluster mass is $M_{\rm ecl,\,min} = 10^3\,{\rm M}_\odot$ (W11). This choice is due to the fact that with high SFR values, the formation of low mass molecular cloud cores may be suppressed due to the intense stellar feedback. However, for $\beta \leq 2$ (as adopted in this paper) the ECMF is not much sensitive to the adopted $M_{\rm ecl,\,min}$ value.
As for the upper mass limit $M_{\rm ecl,\,max}$, following Weidner, Kroupa & Larsen (2004) it can be expressed as:

$$M_{\rm ecl,max} = 8.5 \times 10^4 \left(\frac{\psi(t)}{{\rm M}_\odot\,{\rm yr}^{-1}}\right)^{0.75} {\rm M}_\odot, \quad (3)$$

which holds for both low and high SFRs (Bastian 2008). We fix a maximum value for this upper mass limit at $10^7\,{\rm M}_\odot$, coherently with Weidner et al. (2004).

(ii) Within each embedded stellar cluster of a given mass $M_{\rm ecl}$, the IMF is assumed to be invariant. Following W11, we adopt the multicomponent canonical IMF (Kroupa 2001, 2002), which in its general form is expressed as:

$$\phi(m) = k \begin{cases} k' \left(\frac{m}{m_{\rm H}}\right)^{-\alpha_0} & 0.01 \leq m/M_\odot < 0.08 = m_{\rm H}, \\ \left(\frac{m}{m_{\rm H}}\right)^{-\alpha_1} & 0.08 \leq m/M_\odot < 0.50 = m_0, \\ \left(\frac{m_0}{m_{\rm H}}\right)^{-\alpha_1} \left(\frac{m}{m_0}\right)^{-\alpha_2} & 0.50 \leq m/M_\odot < 1.00 = m_1, \\ \left(\frac{m_0}{m_{\rm H}}\right)^{-\alpha_1} \left(\frac{m_1}{m_0}\right)^{-\alpha_2} \left(\frac{m}{m_1}\right)^{-\alpha_3} & 1.00 \leq m/M_\odot < m_{\rm max}, \end{cases} \quad (4)$$

with the following exponent values:

$$\alpha_0 = +0.30, \quad \alpha_1 = +1.30, \quad \alpha_2 = +2.35, \quad \alpha_3 = +2.35.$$

k and k' are normalization constants whereby the brown dwarf regime need not be a continuous extension of the stellar regime (Thies et al. 2015). In previous chemical evolution studies involving the IGIMF formalism, the quantity α_3 has been kept equal to 2.35, independently from the cluster mass (e.g. Recchi et al. 2009; Calura et al. 2010). As in W11, for clusters with masses $M_{\rm ecl} > 2 \times 10^5\,{\rm M}_\odot$, the exponent α_3 is parametrized as:

$$\alpha_3(M_{\rm ecl}) = \begin{cases} -1.67\,\log_{10}\left(\frac{M_{\rm ecl}}{10^6\,{\rm M}_\odot}\right) + 1.05 & (M_{\rm ecl} \leq 10^6\,{\rm M}_\odot), \\ +1 (M_{\rm ecl} > 10^6\,{\rm M}_\odot). \end{cases} \quad (5)$$

The upper stellar mass limit $m_{\rm max}$ is computed from the mass of the embedded cluster $M_{\rm ecl}$, but in any case is always assumed $\leq 150\,{\rm M}_\odot$ (see Weidner & Kroupa 2004 for more details).

In this study, a metallicity dependence of the IGIMF is not taken into account (see Recchi et al. 2014; Vincenzo et al. 2015; Yan et al. 2019). The adoption of a metallicity-dependent IGIMF (Jeřábková et al. 2018) in high redshift starburst galaxies might be the subject of a future work.

2.1.1 *IGIMF behaviour as a function of β and SFR*

In Fig. 1, we show the IGIMF obtained with our prescriptions and for different values of the SFR, in which we have selected three values of β among those adopted in W11: $\beta = 1$, $\beta = 1.6$, and $\beta = 2$.

We do not consider the most extreme values such as $\beta = 0.5$ and $\beta = 2.35$. By adopting an ECMF with $\beta = 1$ we obtain, for $\psi \gtrsim 10\,{\rm M}_\odot\,{\rm yr}^{-1}$, an IMF comparable to the single-slope IMF of Gibson & Matteucci (1997), a quite extreme top-heavy one (characterized by an index $x = 0.8$ ($x = \alpha - 1$, where $\alpha = 2.35$ is the Salpeter (1955) IMF index) over the whole stellar mass range). On the other hand, the IGIMF obtained adopting $\beta = 2$ is very similar to the Salpeter (1955) IMF over most of the stellar range, except at very high SFR values ($>100\,{\rm M}_\odot\,{\rm yr}^{-1}$).

The IGIMFs calculated at low SFR values ($1\,{\rm M}_\odot\,{\rm yr}^{-1}$) show a uniform decline with mass and the shape of a double-power law, with a knee located at $0.5\,{\rm M}_\odot$. A cut-off is visible at mass values larger than $\sim$100 $\,{\rm M}_\odot$, where the decrease is steeper and where the behaviour is similar to the IGIMF shown in, e. g. Recchi et al. (2009).

In general, the higher the SFR value, the flatter IGIMF, the higher the relative number of massive stars, as due to increasing $M_{\rm ecl,\,max}$ values with increasing SFR. Moreover, the lower the β value, the stronger the IGIMF dependence on the SFR.

2.2 Chemical evolution model

The model used in this work was originally designed to study the evolution of elliptical galaxies (Matteucci 1994; Pipino et al. 2011; Calura et al. 2014; De Masi et al. 2018). The model has been improved by including the formation, growth, and destruction of dust grains, following Gioannini et al. (2017). This allows us to follow the evolution of the abundances of refractory elements (e.g. Si, Fe) in the gas and dust.

2.2.1 *Chemical evolution model*

In our scheme, elliptical galaxies form from the rapid collapse of a gas cloud with primordial chemical composition, described by an exponential infall law. The galaxy is allowed to evolve as an `open box' into the potential well of a dark matter halo. The initial rapid collapse triggers an intense and rapid star formation (SF) episode, i.e. a starburst, which lasts until a galactic wind, powered by the thermal energy injected by stellar winds and SN explosions, occurs. After that time, the galaxy evolves passively, i.e. with no more SF. This is a good approximation as real early-type galaxies have less than 1 per cent of their stellar population younger than 3 Gyr (Salvador-Rusiñol et al. 2019).

In this scenario, the evolution of a given chemical element i is described by:

$$\dot{G}_i = -\psi(t) X_i(t) + R_i(t) + (\dot{G}_i)_{\rm inf} - (\dot{G}_i)_{\rm out}, \quad (6)$$

where $G_i(t) = X_i(t)\,G(t)$ is the gas mass in the form of an element i normalized to the total baryonic mass $M_{\rm lum}$ and $G(t) = M_{\rm gas}(t)/M_{\rm lum}$ is the fractional mass of gas present in the galaxy at the time t. The quantity $X_i(t)$ represents the abundance fraction in mass of a given element i, with the summation over all elements in the gas mixture being equal to unity.

$R_i(t)$ represents the returned fraction of matter in the form of an element i that the stars eject into the interstellar medium (ISM). This term contains all the nucleosynthesis prescriptions about single

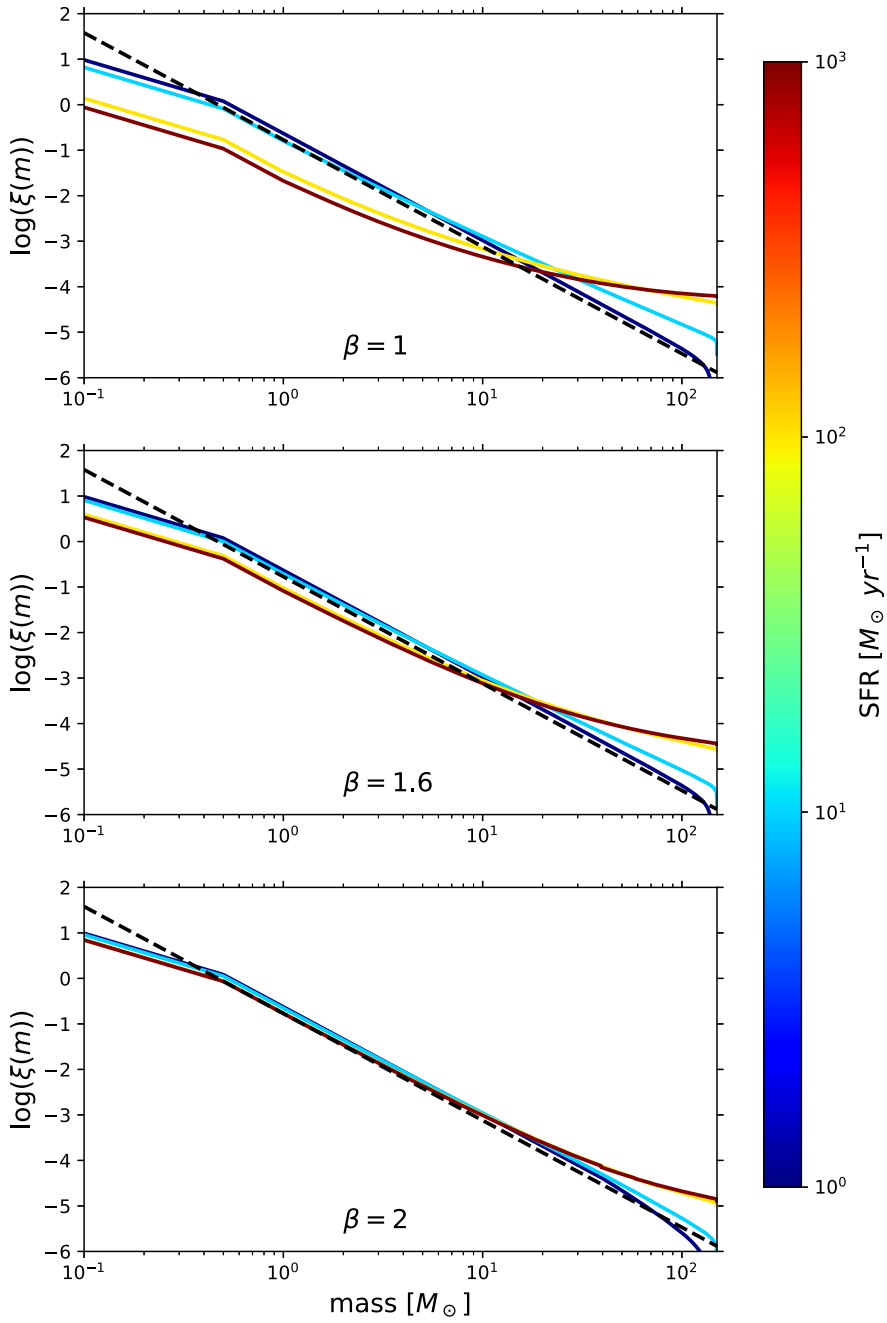

Figure 1. Behaviour of the IGIMF adopted in this paper as a function of stellar mass and SFR for different values of β, namely the slope of the ECMF. Upper panel: $\beta = 1$; central panel: $\beta = 1.6$; lower panel: $\beta = 2$. In each panel, the four solid lines are the IGIMFs computed considering SFR $= 1\,M_\odot\,yr^{-1}$, $10\,M_\odot\,yr^{-1}$, $100\,M_\odot\,yr^{-1}$, $1000\,M_\odot\,yr^{-1}$. The black dashed lines indicate the Salpeter (1955) IMF.

low-intermediate mass stars (LIMS, $m < 8\,M_\odot$), core collapse (CC) SNe (Type II and Ib/c, $m > 8\,M_\odot$), and Type Ia SNe, for which we assume the single-degenerate (SD) scenario. In this scenario, a C-O white dwarf in a binary system accretes mass from a non-degenerate companion until it reaches the Chandrasekhar mass ($\sim$1.44 $M_\odot$) and explodes via C-deflagration. The stellar yields are taken from van den Hoek & Groenewegen (1997) (LIMS), François et al. (2004) (revised version of Woosley & Weaver 1995, for massive stars; for nitrogen see 4.3.1) and Iwamoto et al. (1999) (Type Ia SNe). The fraction of stars in binary systems able to originate Type Ia SNe is fixed at a value able to reproduce the present day Ia SN rate observed in local ellipticals (Matteucci & Recchi 2001; Calura & Matteucci 2006; Pipino & Matteucci 2011).

In equation (6), the term $(\dot{G}_i)_{\rm inf}$ accounts for the infall of external gas. As for the infall, we assume an exponential law:

$$(\dot{G}_i)_{\rm inf} \propto X_{i,\rm inf} \exp(-t/\tau_{\rm inf}), \quad (7)$$

where $X_{i,\rm inf}$ describes the chemical composition of the infalling gas, assumed to be primordial. The quantity $\tau_{\rm inf}$ is the infall time-scale.

The last term of equation (6) represents the galactic wind. The occurrence of the wind is determined by the condition that the thermal energy of the ISM, as due to feedback from SNe and stellar winds, is larger than or equal to the gas binding energy. The feedback prescriptions assumed here are the same as in De Masi et al. (2018): in particular, we assume that only a small, variable fraction (generally of the order of a few per cent) of the initial blast wave energy of CC-SNe, $E_o = 10^{51}$ erg, is deposited in the ISM (see Pipino et al. 2002; Pipino & Matteucci 2004 for details), whereas all the initial blast wave energy of Type Ia SNe (the same as for CC-SNe) is restored into the ISM, as suggested by Recchi, Matteucci & D'Ercole (2001): in fact, when Type Ia SNe explode, the ISM is already hot because of the explosion of CC-SNe. Moreover, we assume that stellar winds by massive stars can inject into the ISM 3 per cent of the typical energy of stellar winds ($\sim 10^{49}$ erg; see Bradamante, Matteucci & D'Ercole 1998 for details).

The dark matter halo is assumed ten times more massive than the luminous mass, with its core radius being ten times larger than the effective radius (see Matteucci 1994; Pipino & Matteucci 2004; De Masi et al. 2018). The large core radius adopted is suggested by observed galaxies but cannot be generated in self-consistent dark matter based models of galaxy formation. The value used here can also be interpreted as the natural core radius of Milgromian potentials, i.e. the phantom dark matter potential generated by the baryonic component (e.g. Lüghausen et al. 2013; Lüghausen, Famaey & Kroupa 2015) is shown in the three figures with the multiple panels of Section 4, in particular in the bottom right-hand panels. In each of those panels, the binding energy (solid line) is computed from the amount of gas and dark matter available in the galaxy, whereas the thermal energy (dashed line) is the cumulative energy deposited by stellar winds and SNe in the gas.

The SFR is calculated as:

$$\psi(t) = \nu G(t), \tag{8}$$

i.e. it is assumed to be proportional to the gas mass via a constant ν, the star formation efficiency, according to the Schmidt–Kennicutt law (Schmidt 1959; Kennicutt 1998). As in the 'inverse wind model' of Matteucci (1994), the star formation efficiency is allowed to vary, increasing with galactic mass. This allows to reproduce the 'downsizing' behaviour of galaxies, with a galactic wind occurring at earlier times in more massive systems, thus producing higher α-elements relative to Fe abundance ratios in the stellar populations of the most massive galaxies, in agreement with observations (see also De Masi et al. 2018).

In the remainder of the paper, we will compare the results obtained with the IGIMF described in Section 2.1 with those obtained with a standard Salpeter (1955) IMF, expressed by a single power law as $\xi(m) \propto m^{-2.35}$.

The main features of the models used in this paper are summarized in Table 1. In the first column, the name of the model is shown. The second column shows the adopted total baryonic mass. The third, the fourth, and the fifth columns indicate for each model the adopted effective radius, the star formation efficiency, and the infall time-scale, respectively.

Table 1. Main parameters assumed for our chemical evolution models for starburst galaxies.

Model name	$M_{\rm lum}$ ($M_\odot$)	$R_{\rm eff}$ (kpc)	ν (Gyr^{-1})	$\tau_{\rm inf}$ (Gyr)
M3E10	3×10^{10}	2	5	0.5
M1E11	1×10^{11}	3	10	0.4
M1E12	1×10^{12}	10	20	0.2

2.2.2 *Dust evolution model*

The chemical evolution model also follows in detail the various processes (production, growth, destruction) that influence dust evolution. Here we adopt the same formalism as used in previous works on chemical evolution models with dust (e.g. Dwek 1998; Calura, Pipino & Matteucci 2008; Vladilo et al. 2018; Palla et al. 2020).

For a specific element i in the dust phase we have:

$$\dot{G}_{i,\rm dust} = -\psi(t) X_{i,\rm dust}(t) + \delta_i R_i(t) + G_{i,\rm dust}(t)/\tau_{i,\rm accr} + \\ - G_{i,\rm dust}(t)/\tau_{i,\rm destr} - \dot{G}_{i,\rm dust,w}(t), \tag{9}$$

where $G_{i,\rm dust}$ and $X_{i,\rm dust}$ are the normalized dust mass and the abundance in dust in the form of an element i, respectively.

Equation (9) includes dust production from AGB stars and CC-SNe (expressed by the rate $\delta_i R_i$), dust growth from refractory elements in the gas phase in the cold ISM (with a rate $G_{i,\rm dust}/\tau_{i,\rm accr}$) and destruction by SNe forward shocks (expressed by $G_{i,\rm dust}/\tau_{i,\rm destr}$).

As for dust production, we use the metallicity-dependent prescriptions from Bianchi & Schneider (2007) for CC-SNe and Dell'Agli et al. (2017) for AGB stars. We also test the role of the reverse shock in the dust yields of CC-SNe. In SN ejecta, the role of the reverse shock in the evolution of the dust deserves particular attention, as in some studies it may destroy large amounts of the dust mass initially produced (e.g. Bianchi & Schneider 2007). To better investigate this aspect, we run a few models which include the reverse shock, and a few ones which do not include it.

At variance with previous works on chemical evolution in elliptical galaxies (Pipino et al. 2011; Grieco et al. 2014), we assume that Type Ia SNe do not produce dust. This assumption is supported both by theoretical and observational arguments (Nozawa et al. 2011; Gomez et al. 2012).

Concerning the processes of growth and destruction, we calculate the metallicity-dependent time-scales $\tau_{i,\rm accr}$, $\tau_{i,\rm destr}$ as in Asano et al. (2013). $\tau_{i,\rm accr}$ depends on the temperature T, density n_H, metallicity Z and grain size a:

$$\tau_{i,\rm accr} \propto \frac{1}{a \cdot n_H \cdot Z \cdot T}, \tag{10}$$

where we assume the reference values of $n_H = 100\,{\rm cm}^{-3}$ (dust condensation takes place in dense gas), $a = 0.1\,\mu$m, $T = 50$ K (as suggested by Asano et al. 2013). As for destruction by SNe, instead, we have:

$$\tau_{i,\rm destr} \propto \frac{1}{\epsilon \cdot M_{\rm swept} \cdot SN_{\rm rate}}, \tag{11}$$

where we assume an efficiency of destruction $\epsilon = 0.1$ (as suggested by Asano et al. 2013) and a swept mass by SN forward shock $M_{\rm swept}$ dependent on metallicity Z.

Because of the uncertainties related to dust growth in the ISM, we also run models without any dust growth in the ISM. In fact, it was shown that dust condensation in high redshift galaxies can encounter theoretical problems (Ferrara, Viti & Ceccarelli 2016), as the large amount of UV radiation from massive stars in starbursts can impact on the net dust growth rate (Gall & Hjorth 2018). On

Table 2. Main features of the sample of starburst galaxies included in our sample. Objects in the upper part of the table (i.e. above the horizontal line) are lensed galaxies. Objects below the line are stacked spectra of galaxies.

Object	Redshift	SFR ($M_\odot$ yr^{-1})	M_* ($M_\odot$)	Notes	References
MS 1512-cB58	2.7276	∼25–∼150	$\sim10^{10}$	(1), (2), (3)	Pettini et al.(2000, 2002); Teplitz et al. (2000); Siana et al. (2008)
8 o'clock arc	2.7350	∼270	$\sim10^{11.6}$	(2), (3)	Dessauges-Zavadsky et al. (2010); Finkelstein et al. (2009)
Cosmic Horseshoe	2.3812	∼95–∼190	$\sim10^{10}$	(1), (2), (3)	Quider et al. (2009); Hainline et al. (2009)
SGAS J105039.6+001730	3.6252	∼90–∼140	$\sim10^{9.7}$	(2)	Bayliss et al. (2014)
RCSGA 032727-132609	1.7037	∼130–∼360	$\sim10^{10.3}$	(2)	Wuyts et al. (2010); Rigby et al. (2011)
SMACS J0304.3-4402	1.96	∼20–∼90	$\sim10^{10.8}$	(2)	Christensen et al.(2012a,b)
SMACS J2031.8-4036	3.51	∼15–∼30	$\sim10^{9.4}$	(2)	Christensen et al.(2012a,b)
KBSS-LM1 Composite	2.396 ± 0.111	∼50–∼55	$\sim10^{10}$	(2), (4)	Steidel et al. (2016)
Shapley LBG Composite	∼3	>50	–	(2)	Shapley et al. (2003); Pettini et al. (2001)

Notes. SFR and M_* estimates were derived adopting a Salpeter (1955) IMF.
(1) M_* is the baryonic mass; (2) abundances from emission lines; (3) abundances from absorption lines; (4) median values of the sample, except for redshift (medium value with rms of the sample).

the other hand, grain growth in the ISM is also required to explain the large depletion rates of Fe, whose main producers (Type Ia SNe) do not seem to contribute to dust production (e.g. Nittler et al. 2018).

At the same time, we also test models without forward shock destruction by SNe. In fact, the impact of these phenomena on the dust survival rate is still a matter of debate (Gall & Hjorth 2018 and references therein).

In our plots, the results of our models which include the various processes of dust production, growth, and destruction are dubbed as follows. All the models which include reverse shocks in SNe are labelled with 'R', and models in which reverse shock is turned off are labelled 'NR'. Models which include growth (accretion) and destruction are labelled 'A' and 'D', respectively. As examples, a model which includes reverse shock, growth, and destruction will be 'ADR', whereas a model in which growth and destruction are absent but reverse shock is present will be dubbed 'R'.

3 OBSERVATIONAL DATA

In Tables 2 and 3 we list the observed systems selected for this study with their main features (redshift, SFR, stellar mass) and their chemical abundances.

In our analysis, we consider several lensed objects (LBGs and Lyα emitters) (upper parts of Tables 2 and 3). The magnification due to gravitational lensing allows one to perform high-quality spectroscopy, from which physical properties and chemical abundances can be derived from high S/N data (Bayliss et al. 2014 and references therein).

We extend our sample of high-redshift star-forming systems by considering also two cases where 'composite' spectra from sizable sets of high-z systems were obtained with observations in non-lensed fields. The data for composite samples are reported in the lower part of Tables 2 and 3. These samples include high-redshift systems, with average stellar masses and SFR values comparable to the ones of the lensed objects. In the following, we will give a brief description of each of the objects considered in our analysis.

3.1 MS 1512-cB58

MS 1512-cB58 (hereafter, cB58) is a lensed LBG first discovered by Yee et al. (1996), with redshift $z = 2.7276$ (Pettini et al. 2002). It is magnified by a factor ∼30 by the cluster MS 1512+36 at $z = 0.37$ (Pettini et al. 2000).

Several SFR estimates were performed for this object in the past years, leading to different results depending on the adopted SFR estimator (e.g. IR, Hα, UV). The available values span the range $\sim25 - \sim150\,M_\odot$ yr^{-1} (Siana et al. 2008). As noted by Siana et al. (2008), however, the highest SFR values might represent upper limits due to overestimated extinction corrections.

The estimated baryonic mass is of the order of $\sim10^{10}\,M_\odot$ (Pettini et al. 2000; Baker et al. 2004), whereas the effective radius is $R_{\rm eff} \sim 2$ kpc (Seitz et al. 1998).

The observed abundances in Table 3 are from Teplitz et al. (2000) and Pettini et al. (2002). The 12+log(O/H) and log (N/O) abundances were estimated by Teplitz et al. (2000) from interstellar emission lines. The O abundance was calculated by means of the R_{23} indicator. The abundances obtained by Pettini et al. (2002) were computed from interstellar absorption lines, and in particular from the measured column densities using the apparent optical depth method. The N/O values from both sets will be compared with the models, in order to appreciate the differences in the measures as obtained from emission and absorption lines.

3.2 8 o'clock arc

The 8 o'clock arc is an LBG at redshift $z = 2.7350$, lensed by the luminous red galaxy (LRG) SDSS J002240.91+143110.4 at $z = 0.38$ (Allam et al. 2007). The arc has an inferred stellar mass of $4.2 \times 10^{11}\,M_\odot$ and an SFR of $266 \pm 74\,M_\odot$ yr^{-1} (corrected for a lensing magnification of $\mu = 8$, Finkelstein et al. 2009). Analysis of the Baldwin–Phillips–Terlevich (BPT) diagram excludes substantial AGN contamination (Finkelstein et al. 2009).

In Table 3, we show the O abundances from the Keck/LRIS emission spectrum (Finkelstein et al. 2009) and the Fe, Si abundances obtained from the VLT/X-Shooter absorption spectrum of Dessauges-Zavadsky et al. (2010). O abundances are obtained from the N_2 indicator, whereas Fe, Si abundances by means of the apparent optical depth method (as in Pettini et al. 2002).

3.3 Cosmic horseshoe

The cosmic horseshoe is a gravitationally lensed LBG discovered by Belokurov et al. (2007), with redshift $z = 2.3812$. It is magnified by a factor $\mu = 24 \pm 2$ by a massive LRG at $z = 0.444$ (Dye et al. 2008). The inferred baryonic mass and effective radius are of the

Table 3. Abundance ratios of starburst galaxies included in our sample. Objects above the line are lensed galaxies. Objects below the line are stacked spectra of galaxies. In parentheses, the method of estimation for log (O/H)+12 is indicated.

Object	log(O/H)+12	log(N/O)	log(C/O)	[Fe/H][1]	[Si/H][1]	[Mg/H][1]
MS 1512-cB58	8.39 ± 0.10 (R_{23})	-1.24 ± 0.14 (Teplitz et al. 2000) -1.89 ± 0.14 (Pettini et al. 2002)	–	-1.15 ± 0.1	-0.37 ± 0.1	-0.32 ± 0.1
8 o'clock arc	8.58 ± 0.18 (N_2)	–	–	-0.93 ± 0.15	-0.19 ± 0.14	–
Cosmic Horseshoe	8.38 ± 0.18 (N_2)	–	–	$-1.17^{+0.18}_{-0.15}$	$-0.29^{+0.18}_{-0.15}$	–
SGAS J105039.6+001730	$\geq$8.05 (direct) 8.17 ± 0.12 (R_{23})	-1.59 ± 0.2	-0.79 ± 0.06	–	–	–
RCSGA 032727-132609	$\geq$8.14 (direct) 8.20 ± 0.08 (R_{23}) 8.20 ± 0.04 (N_2)	1.7 ± 0.02	–	–	–	–
SMACS J0304.3-4402	8.07 ± 0.09 (direct) 8.16 ± 0.01 (R_{23})	-1.64 ± 0.05	–	–	–	–
SMACS J2031.8-4036	7.76 ± 0.03 (direct) 7.74 ± 0.03 (R_{23})	–	-0.80 ± 0.09	–	–	–
KBSS-LM1 Composite	8.38 ± 0.05 (direct) 8.20 ± 0.1 (R_{23}) 8.32 ± 0.05 (N_2)	-1.24 ± 0.04	-0.60 ± 0.09	–	–	–
Shapley LBG Composite	[7.64,8.73] (R_{23})	–	[−0.81, −0.56]	–	–	–

Note. [1] $[X/Y] = \log(X/Y) - \log(X_\odot/Y_\odot)$, where X, Y are abundances in the ISM for the object studied and $X_\odot$, $Y_\odot$ are solar abundances (from Asplund et al. 2009).

order of $10^{10}\,M_\odot$ and 2.5 kpc (Hainline et al. 2009), respectively. Its H_α and UV luminosities yield SFR values of $95\,M_\odot\,yr^{-1}$ (Quider et al. 2009) and $190\,M_\odot\,yr^{-1}$ (Hainline et al. 2009), respectively.

The absorption lines from its Keck II/ESI spectrum (Quider et al. 2009) and the emission lines from Keck II/NIRSPEC (Hainline et al. 2009) give the abundances presented in Table 3. The abundances for Fe and Si were obtained by means of the apparent optical depth method, whereas its O abundance from the N_2 indicator.

3.4 SGAS J105039.6+001730

The SGAS J105039.6+001730 LBG at redshift $z = 3.6252$ is a system lensed by a foreground galaxy cluster at $z = 0.593$. The lensing magnification is of the order of ∼30. By taking into account the magnification factor, Bayliss et al. (2014) derived for the galaxy a stellar mass of $5 \times 10^9\,M_\odot$ and values of the SFR between 90 and $140\,M_\odot\,yr^{-1}$ (depending if based on [OII] or H_β luminosity, respectively). The Magellan/FIRE interstellar emission spectrum ruled out a substantial AGN contribution.

Abundances in Table 3 are taken from Magellan/FIRE spectrum (Bayliss et al. 2014). As for the O abundance, both the direct measure and the value inferred via the R_{23} indicator are presented.

3.5 RCSGA 032727-132609

RCSGA 032727-132609 is a bright lensed galaxy (at the time of its discovery, it was the most luminous lensed galaxy ever known) at redshift $z = 1.7037$, magnified by a factor $\mu = 17.2 \pm 1.4$ by RCS2 032727-132623 galaxy cluster at $z = 0.564$. From spectral energy distribution (SED) fitting, the stellar mass was found to be $2 \times 10^{10}\,M_\odot$ (Wuyts et al. 2010). Different methods give SFR values between $\sim 130\,M_\odot\,yr^{-1}$ (Wuyts et al. 2010) and $\sim 360\,M_\odot\,yr^{-1}$ (Rigby et al. 2011). As noted in Rigby et al. (2011), the highest SFR value is to be regarded as an upper limit. The BPT diagram for this object is consistent with no AGN contribution.

The abundances in Table 3 are taken from Keck II/NIRSPEC emission spectrum (Rigby et al. 2011). The log (O/H)+12 values reported in Table 3 refer to the direct, R_{23} and N_2 methods. Other abundance indicators (e.g. N_3O_2) were used to estimate its metallicity (Rigby et al. 2011), with derived values which are similar to the ones shown in Table 3.

3.6 SMACS J0304.3-4402

This Lyα emitter at redshift $z = 1.963$ is magnified by a factor $\mu = 42.0 \pm 8.0$ by a galaxy cluster placed between redshift 0.3 and 0.5 (Christensen et al. 2012a). SED fitting reveals a stellar mass of $6.3 \times 10^{10}\,M_\odot$. The inferred SFR from emission lines lies between ∼20 (friom the H_α-detection) and $\sim 90\,M_\odot\,yr^{-1}$ (from the [OII]-detection). The rest-frame UV spectrum shows no AGN contribution.

The abundance ratios presented in Table 3 are from the VLT/X-Shooter emission line spectrum by Christensen et al. (2012a,b). O/H has been measured using both direct and R_{23} methods.

3.7 SMACS J2031.8-4036

SMACS J2031.8-4036 is a Lyα emitter at redshift $z = 3.51$. It is magnified by a factor $\mu = 15.8 \pm 7.0$ by a galaxy cluster at $z = 0.331$ (Christensen et al. 2012a). The SED fitting reveals a stellar mass of $2.4 \times 10^9\,M_\odot$. Its VLT/X-Shooter emission line spectrum indicates no AGN contribution and an SFR between ∼15 and $\sim 30\,M_\odot\,yr^{-1}$, inferred via [OII] and H_α detection, respectively (Christensen et al. 2012a,b).

The abundance data in Table 3 were derived from the VLT/X-Shooter spectrum. The two values for log (O/H)+12 are estimated by means of the direct and the R_{23} methods.

3.8 KBSS - LM1 (composite)

This composite spectrum is the result of the combined analysis of Keck/LRIS and Keck/MOSFIRE observations of a sample of 30 galaxies from the KBSS-MOSFIRE survey (Steidel et al. 2014).

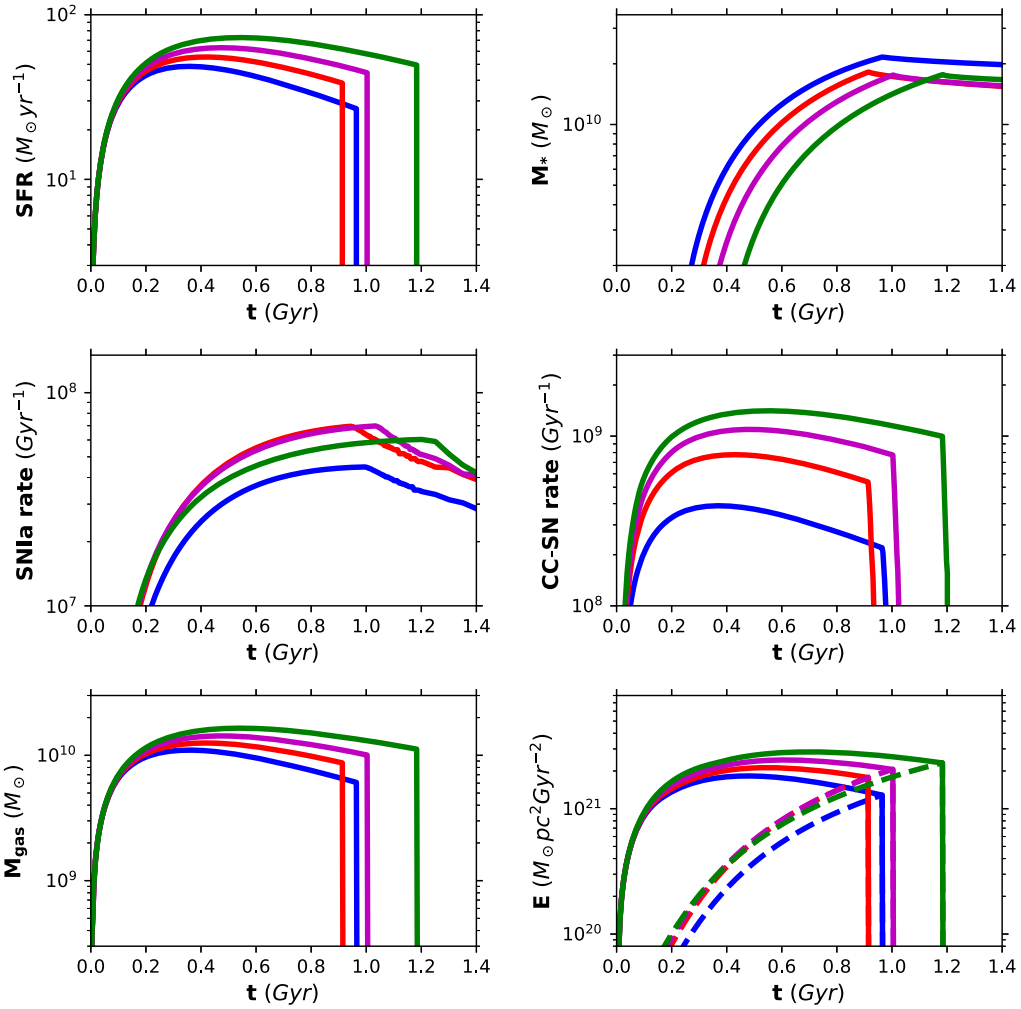

Figure 2. From top-left corner, clockwise: time evolution of the SFRs, stellar mass, CC-SN rate, energetic budget, gas mass, and Type Ia SN rates obtained for the M3E10 model (see Table 1) with a Salpeter (1955) IMF (blue lines) and W11 IGIMF calculated for $\beta = 1$ (green lines), $\beta = 1.6$ (magenta lines) and $\beta = 2$ (red lines). The sharp truncation in the SFR, CC-SN rate, and gas mass are due to the onset of the galactic wind, which devoids the galaxy from the residual gas. In the energetic budget plot, the solid lines represent the binding energy and the dashed lines the thermal energy in all the different models.

Galaxies of this subsample lie in the redshift range $2.113 \leq z \leq 2.572$, which is optimal to get access to nebular lines as well as integrated OB stars light. Median values of the stellar mass and the SFR are $\log(M_*/M_\odot) \simeq 10.0$ and $\sim 50\,M_\odot\,yr^{-1}$, as traced by UV and H_α indicators, respectively.

The abundances shown in Table 3 are taken from Steidel et al. (2016). The three (O/H) values are from different estimators, namely the direct, the R_{23}, and the N_2 methods. The direct measurement value is consistent with the one constrained from SED fitting (Steidel et al. 2016).

3.9 Shapley+03 LBG (composite)

Shapley et al. (2003) consider a sample of almost 1000 LBGs at redshift $z \sim 3$ with spectra taken with Keck/LRIS. In general, the emission line stacked spectrum shows vigorous SF. All the four subsamples in which the full sample of galaxies is divided show $SFR > 50\,M_\odot\,yr^{-1}$. No evidence of AGN emission is found in the composite spectrum.

In Table 3 we show the abundances derived by Shapley et al. (2003). The O/H abundance is taken from a sample of LBGs originally presented in Pettini et al. (2001).

4 RESULTS

4.1 The effects of the IGIMF on the galactic star formation history

In Figs 2–4 we show the impact of the IMF on the evolution of the SFR, Type Ia, and CC-SN rates, as well as gas, stellar mass, and energetic budget for the starburst models of Table 1.

All the models presented in Figs 2–4 are characterized by SF efficiencies of 5, 10, and $20\,Gyr^{-1}$, respectively. The fact that in each figure the SF efficiency is constant allows us to single out the effects of the IMF on the global properties of the galaxy of that particular mass.

The star formation histories reported in Figs 2–4 are strongly dependent on the adopted IMF.

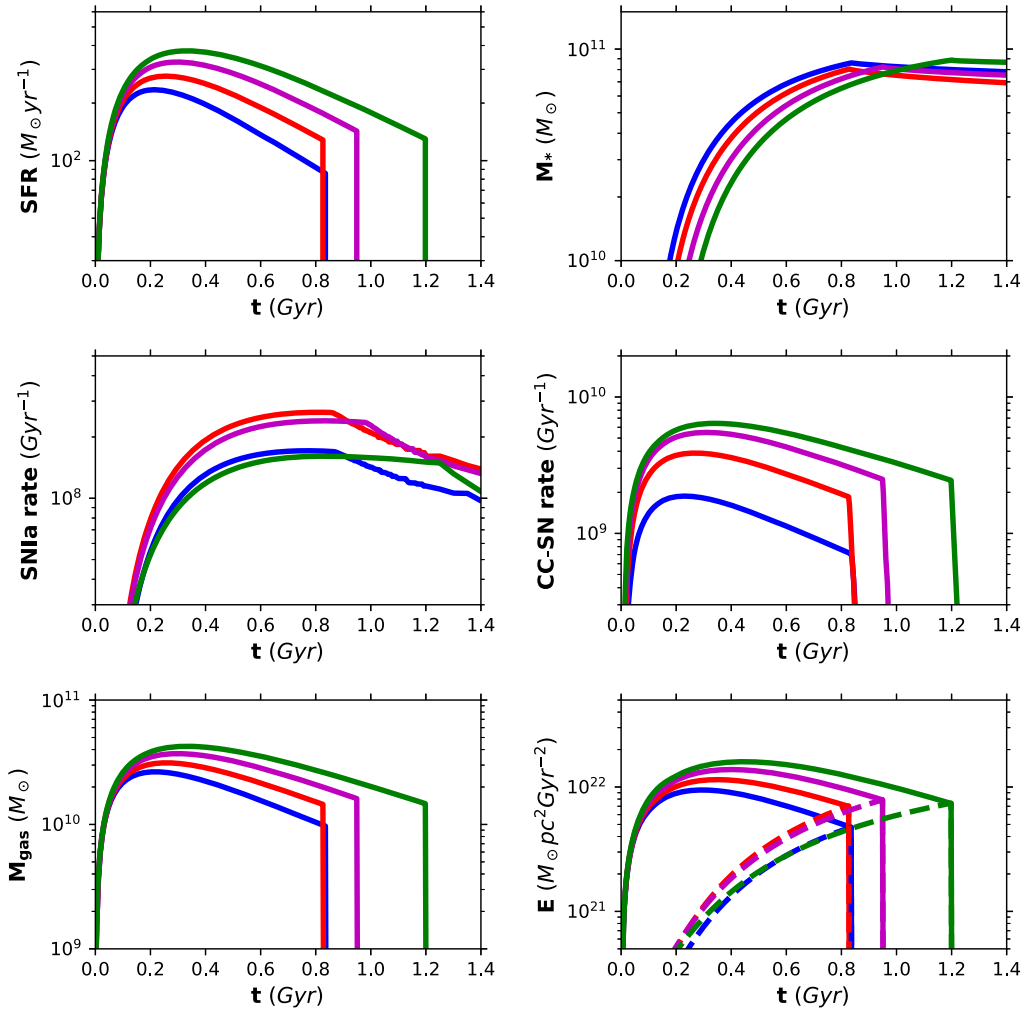

Figure 3. Lines are as in Fig. 2, but computed for the M1E11 model of Table 1.

In general, the models computed adopting the W11 IGIMF exhibit larger SFR values than the ones computed with a Salpeter IMF. This can be explained by the fact that a top-heavy IMF implies larger mass ejection rates from evolved stellar populations, and in particular from massive stars, with consequently larger gas mass reservoirs at any time, which also imply larger SFR values.

The differences in the star formation histories caused by the adopted IMF determine also the conditions for the onset of a galactic wind, and consequently the time at which the star formation stops. We note that the steepest IGMFs ($\beta = 1.6$ and $\beta = 2$) produce winds at the earliest times. In the case $\beta = 1$, in spite of the very high number of CC-SNe (which is roughly proportional to the SFR), the galactic wind occurs later than in the cases with $\beta > 1$ because of the larger binding energy of the gas compared to the other models (see Section 2.2).

By comparing Figs 2 and 3, it is worth noting that a later occurrence of galactic winds in less massive galaxies, i.e . the downsizing in star formation as obtained by Matteucci (1994) by means of the inverse wind model, cannot be reproduced by adopting the IGIMF with $\beta = 1$, and this occurs despite a higher star formation efficiency for the larger mass model. It is worth reminding that the inverse wind model can reproduce the observed increase of the integrated [α/Fe] with galactic stellar mass in ellipticals (see Thomas et al. 2010).

In Matteucci (1994) the winds concurring at earlier times in massive galaxies were obtained by increasing the efficiency of SF with galactic stellar mass, as we assume here, and with a constant Salpeter IMF. The inverse wind effect is visible from the models for the Salpeter IMF as well as for the case $\beta = 2$ and $\beta = 1.6$.

In Fig. 4 the behaviour of M1E12 models is shown. The results are very similar to what found for M1E11 models. The same trends shown by the M1E11 and M1E12 models are explained by the similar IGIMFs, in particular at $\psi > 100\,M_\odot\,yr^{-1}$ (see Fig. 1). The assumption of an upper mass limit for the maximum mass of stellar clusters ($M_{ecl,\,max}$) attenuates the dependence of the IGIMF on the SFR at very high ψ values ($\gtrsim 500\,M_\odot\,yr^{-1}$).

Looking at the lower left-hand panel in Fig. 4, it is visible that large amounts of gas are restored into the ISM after the onset of the galactic wind. The same behaviour is not shown by the lower mass models (Figs 2 and 3), where the thermal energy of the gas after the galactic wind is always larger than its binding energy.

Another interesting aspect of Fig. 4 is that the model with $\beta = 1$ gives a Type Ia SN rate which is lower than the one obtained with the Salpeter IMF, at variance with what is shown in Figs 2 and, although to a lesser extent, 3. This is expected from Fig. 1, where we have seen that the most extreme differences between the Salpeter IMF and the IGIMF were found when the lowest value for β was adopted and at the highest SFR values. Under such extreme

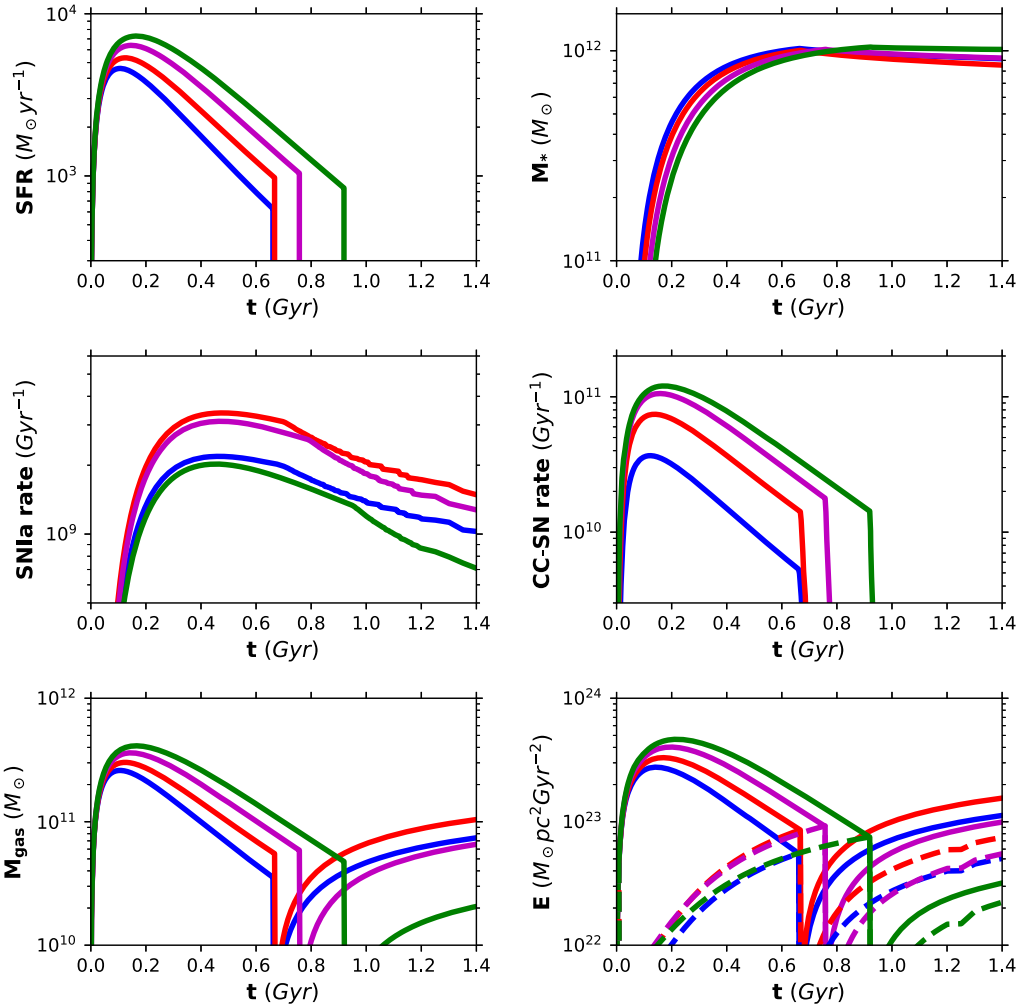

Figure 4. Lines are as in Fig. 2, but computed for the M1E12 model of Table 1.

conditions, an IMF remarkably light in low- and intermediate-mass stars, i. e. in the mass range of the progenitors of Type Ia SNe, is possible.

4.2 The effects of the IGIMF on chemical abundances

In Fig. 5, we show the [O/Fe] versus [Fe/H] plots computed for the M3E10 models with the IGIMF and with different values of β (green, red, and magenta lines) as well as for the M3E10, M1E11, M1E12 models with a Salpeter (1955) IMF (blue lines).

From this Figure we can see that in general, at any time the W11 IGIMF produces larger [O/Fe] values than the Salpeter (1955) IMF.

These features can be seen from the different levels of the plateau in the [O/Fe]-[Fe/H] relation obtained with the M3E10 model assuming different IMFs. At low metallicity ([Fe/H] ≤ -1.5), higher [O/Fe] values are obtained assuming lower β values (i.e. with IMFs heavier in massive stars). Also the slope of the [O/Fe]-[Fe/H] relation is dependent on the IMF, with a steeper decrease for higher values of β.

A larger extension of the plateau for lower β values is again due to a larger number of massive stars, which are the first to enrich the ISM with Fe. The larger the fraction of massive stars, the higher the metallicity value (as traced by [Fe/H]) at which Type Ia SNe start to contribute significantly to the Fe enrichment, thus the higher is the [Fe/H] value for the change in slope of the [O/Fe]-[Fe/H] relation. This is a known consequence of the 'time-delay model' (Matteucci 2012). We also note that in the IGIMF models, a value of [α/Fe] larger by 0.2 dex as traced by O extends to much higher metallicity values than with the Salpeter IMF, reaching values as high as [Fe/H]$\sim$ 0.4.

The [O/Fe]-[Fe/H] plots for the models M1E11 and M1E12 computed adopting the IGIMF with different β values are very similar to Fig. 5, hence they are not shown here. For comparison, we show only the results of the M1E11 and M1E12 models obtained for a Salpeter IMF, to stress that an increase in galactic mass and in SF efficiency leads to an increase of the [O/Fe] value at [Fe/H] $= -2$, without affecting in a substantial way the slope of the [O/Fe]-[Fe/H] relation.

4.3 A direct comparison with high redshift starbursts

We will now compare the abundance patterns obtained by means of chemical evolution models adopting different IMF prescriptions with the observed abundances of Table 3.

We will divide the discussion into two parts. First, we will study the behaviour of abundance ratios of volatile elements, namely the elements which are negligibly affected by the presence of dust (such as N and O). Then, we will discuss abundance ratios

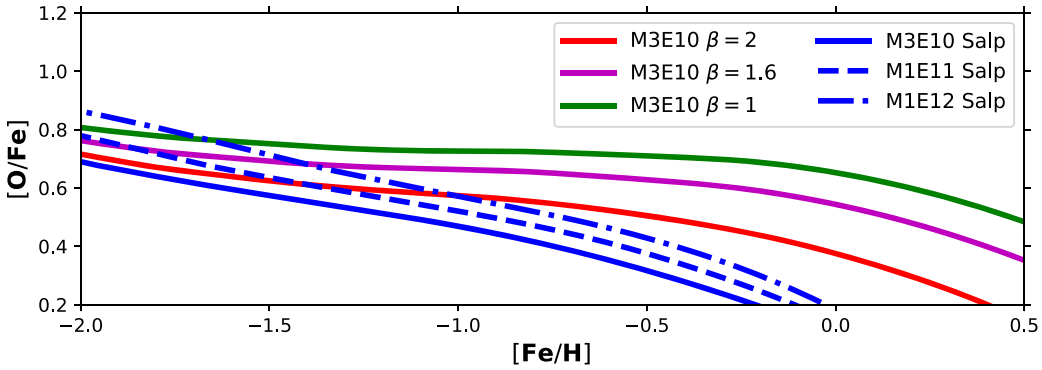

Figure 5. Evolution of the interstellar [O/Fe] versus [Fe/H] relation. Lines are computed for: M3E10 models (solid) with Salpeter (1955) IMF (blue) and W11 IGIMF calculated for $\beta = 1$ (green), $\beta = 1.6$ (magenta) and $\beta = 2$ (red); M1E11 model with Salpeter (1955) IMF (dashed blue); M1E12 model with Salpeter (1955) IMF (dash-dotted blue).

between refractory elements, i.e. elements severely affected by dust depletion (such as C, Mg, Si, Fe), and compare data with model abundances.

4.3.1 Volatile element ratios

We start our analysis from the (N/O) versus (O/H) relation, visible in Fig. 6. The analysis of N deserves a special attention, since its origin is still debated.

For this reason, in the two plots of Fig. 6 we show models with different N yields: the Matteucci (1986) (thick lines) and the Meynet & Maeder (2002) (thin lines) ones. The former set assumes that all massive stars produce primary[2] N, an ad hoc hypothesis that is necessary to explain the high (N/O) ratios observed in low metallicity MW halo stars (Israelian et al. 2004; Spite et al. 2005; see also Vincenzo & Kobayashi 2018).

The Meynet & Maeder (2002) yields, instead, allow for the production of primary N only in rotating, massive, very low metallicity stars. In general, this leads to a deficiency of N between low and intermediate metallicities (Romano et al. 2010; Vincenzo et al. 2016), at variance with observations. As for observational data, it is worth stressing that the variation in log (O/H)+12 for a given system due to a different metallicity indicator is typically $\leq$0.2 dex. As for the theoretical abundances, here we show only the results obtained for the M3E10 and M1E11 models.

As shown in Fig. 6, in the case of the yields for primary N of Matteucci (1986), the adoption of the IGIMF leads to lower (N/O) values at metallicity log (O/H)+12 $>$ 7 with respect to the Salpeter model. At lower metallicity, very small variations due to different IMFs are visible in the case of the M3E10 model (upper panel in Fig. 6).

The variations between the abundances obtained with the Salpeter IMF and the ones obtained with the IGIMF increase with metallicity, and in general the lower the β, the larger the variation. A maximum variation of $\sim$0.4 dex between the (N/O) values with Salpeter and IGIMF is visible at log (O/H)+12 = 9 in the case of $\beta = 1$ for the M3E10 model.

At all metallicities, larger (N/O) variations between Salpeter and IGIMF are visible in the case of the M1E11 model, with a maximum

[2]Primary production of an element stems directly from the synthesis of H and He. In the case of secondary production, the seed for the synthesis must be a heavy element (such as O).

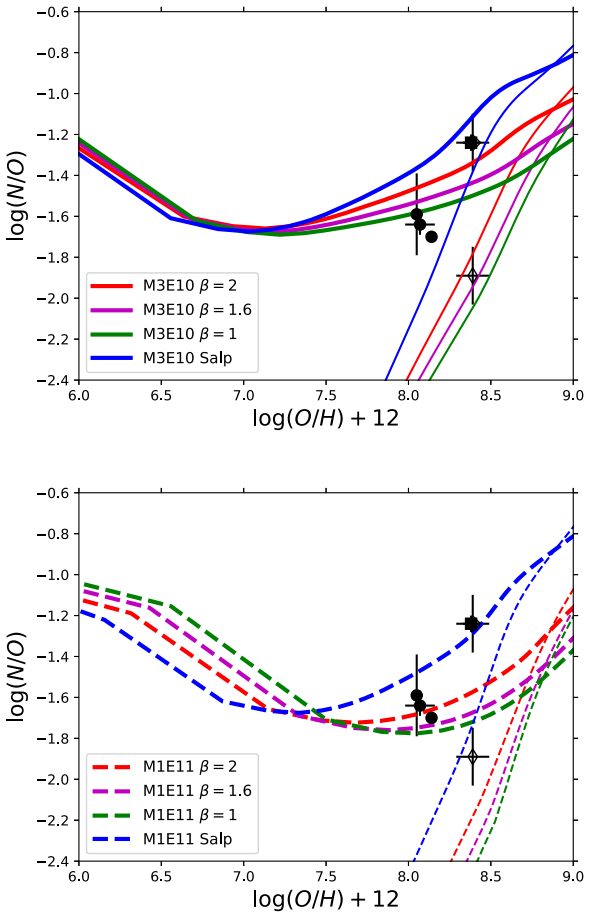

Figure 6. log (N/O) versus log (O/H)+12 adopting Matteucci (1986) yields for N (thick lines) and Meynet & Maeder (2002) (thin lines) compared with abundances measured in galaxies of the sample of Table 3. Upper panel: lines are computed for M3E10 models (solid) with Salpeter (1955) IMF (blue) and W11 IGIMF calculated for $\beta = 1$ (green), $\beta = 1.6$ (magenta) and $\beta = 2$ (red). Lower panel: lines are computed for M1E11 models (dashed) with a Salpeter (1955) IMF (blue) and W11 IGIMF calculated for $\beta = 1$ (green), $\beta = 1.6$ (magenta) and $\beta = 2$ (red). For both panels: data are from Steidel et al. (2016) stacked spectrum (filled square); Rigby et al. (2011), Bayliss et al. (2014), Christensen et al. (2012a,b) (filled circles); Pettini et al. (2002) (thin diamond) and Teplitz et al. (2000) (thick diamond).

value of ∼0.6 at log (O/H)+12 = 9 in the case of $\beta = 1$ (lower panel of Fig. 6).

Similar conclusions can be drawn for the models with the Meynet & Maeder (2002) yields, with a metallicity-dependent increase of the variation between the (N/O) obtained with the Salpeter and the IGIMF.

As for the comparison between the abundances observed in the high-z sample of Table 3 and models, without the primary N yields as suggested by Matteucci (1986) it would be impossible to reproduce the (N/O) values measured in three out of four of the data shown in Fig. 6. This reinforces the results found in previous studies, e. g. on the need of primary N in massive stars to reproduce the (N/O) values measured in star-forming galaxies in the Local Universe (e.g. Vincenzo et al. 2016).

Fig. 6 outlines the role of the adopted IMF in determining the interstellar abundance pattern. In several cases, it is difficult to disentangle between effects due to the IMF and nucleosynthesis prescriptions.

In summary, the comparison between data and model discussed in this section provides useful suggestions regarding the nucleosynthesis of the volatile elements N and O. However, the analysis of the observational data considered here is not conclusive on whether the IGIMF is to be preferred over the Salpeter IMF to reproduce these particular abundance ratios. To this purpose, more insights are provided by the study of the abundance ratios between refractory elements, described in the remainder of this Section.

4.3.2 *Refractory elements abundance ratios*

Figs 7–10 show the calculated (C/O)-(O/H), [Si/Fe]-[Fe/H], [Mg/Fe]-[Fe/H], and [O/Fe]-[Fe/H] relations, respectively, each one computed without taking into account dust depletion in the ISM for M3E10 and M1E11 models, compared to observed abundances from the data set presented in Section 3 . We omit for all the plots the results of the M1E12 model with the IGIMF, as they are characterized by SFR values much larger than the ones observed in the systems of our data set.

We should highlight that none of the observed abundance ratio involving refractory elements is altered by corrections due to reddening/extinction.

In fact, C/O abundances are determined using C3O3 line ratio (Garnett et al. 1995), which is insensitive to reddening corrections, due to the very similar wavelengths of the lines. On the other hand, other refractory elements are generally studied by means of absorption line spectroscopy, with their abundances are just derived from the equivalent width of the lines.

From the (C/O)-(O/H) relation of the M3E10 models (upper panel of Fig. 7) we see that varying the IMF does not produce any significant change in the abundance pattern. In the (C/O)-(O/H) diagram, the effects produced by adopting different IMFs tend to cancel out, thus producing a very similar behaviour of the abundance ratio versus metallicity. Note that all the models fall in the confidence region derived by stacked spectra by Shapley et al. (2003) and the sample of $z \sim 3$ LBGs of Pettini et al. (2001). Similar conclusions can be drawn from the analysis of the results for the M1E11 models, with the only difference that in this case the IGIMF produces higher (C/O) values than Salpeter only at low metallicity (log (O/H)+12 < 7.5), e.g. in the case of $\beta = 1$ higher by up to a few 0.1 dex at log (O/H)+12 ∼ 6.7, with decreasing differences at increasing metallicity. In this case, differences between models with Salpeter and IGIMF are found only outside the observational data range, which does not allow us to prefer any model in particular. Useful information will come later when we will analyse the effects of dust depletion.

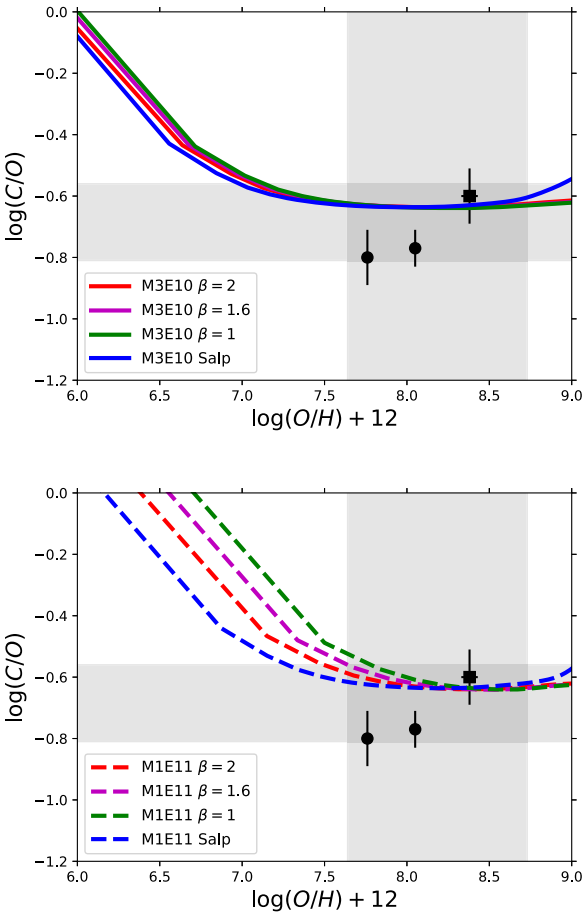

Figure 7. log (C/O) versus log (O/H)+12 computed without taking into account dust depletion and compared with abundances measured in galaxies of the sample of Table 3. Upper panel: lines are computed for M3E10 models (solid) with Salpeter (1955) IMF (blue) and W11 IGIMF calculated for $\beta = 1$ (green), $\beta = 1.6$ (magenta) and $\beta = 2$ (red). Lower panel: lines are computed for M1E11 models (dashed) with Salpeter (1955) IMF (blue) and W11 IGIMF calculated for $\beta = 1$ (green), $\beta = 1.6$ (magenta), and $\beta = 2$ (red). For both panels: the shaded regions indicates the log (C/O) confidence region derived from the composite LBG spectrum of Shapley et al. (2003) and the log (O/H)+12 characterizing the sample of LBGs of Pettini et al. (2001). Other data are from Steidel et al. (2016) stacked spectrum (filled square), Bayliss et al. (2014) and Christensen et al. (2012a,b) (filled circles).

The (C/O) abundances observed in this data set confirm the suitability of the yields we are adopting here, which consider rotation in very massive stars ($m > 40\,M_{\odot}$) at all metallicities (e.g. Chiappini, Romano & Matteucci 2003), also in systems characterized by a star formation history likely much different than the one of the Milky Way.

In the [Si/Fe]-[Fe/H] plot for the M3E10 models (Fig. 8, upper panel), for two data points the theoretical abundances lie below the error bars by 0.1 in the best case, i.e. the models in which the IGIMF is adopted. The M3E10 model with the IGIMF and $\beta = 1$ lies slightly below the highest-metallicity point. A marginal overlap between the error bar of the highest metallicity [Si/Fe] value and the M1E11 model with $\beta \leq 1.6$ is visible in Fig. 8 (bottom panel).

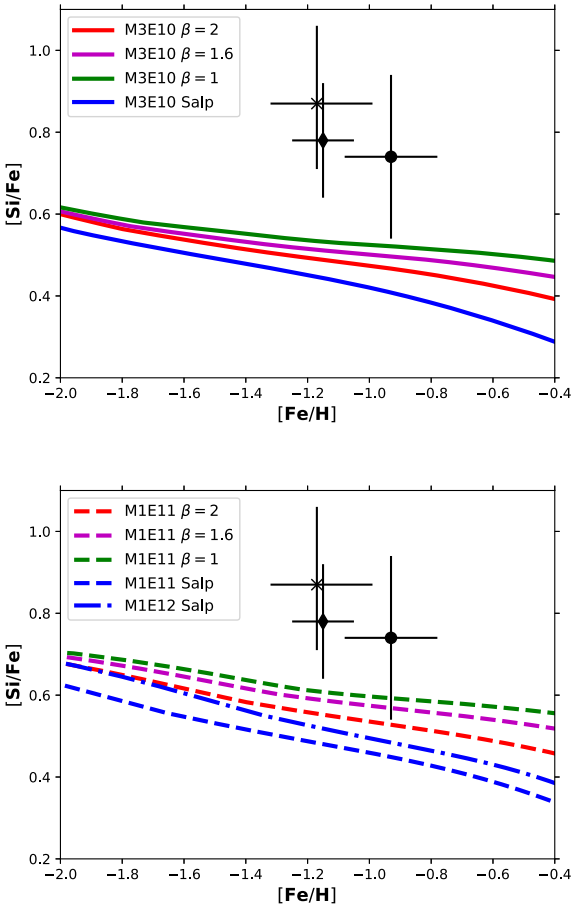

Figure 8. [Si/Fe] versus [Fe/H] computed without taking into account dust depletion and compared with abundances measured in galaxies of the sample of Table 3. Upper panel: lines are computed for M3E10 models (solid) with Salpeter (1955) IMF (blue) and W11 IGIMF calculated for $\beta = 1$ (green), $\beta = 1.6$ (magenta) and $\beta = 2$ (red). Lower panel: lines are computed for M1E11 models (dashed) with Salpeter (1955) IMF (blue), W11 IGIMF calculated for $\beta = 1$ (green), $\beta = 1.6$ (magenta) and $\beta = 2$ (red); M1E12 model with Salpeter (1955) (blue dash-dotted). For both panels: data are from Pettini et al. (2002) (diamond); Quider et al. (2009) (cross); Dessauges-Zavadsky et al. (2010) (filled circle).

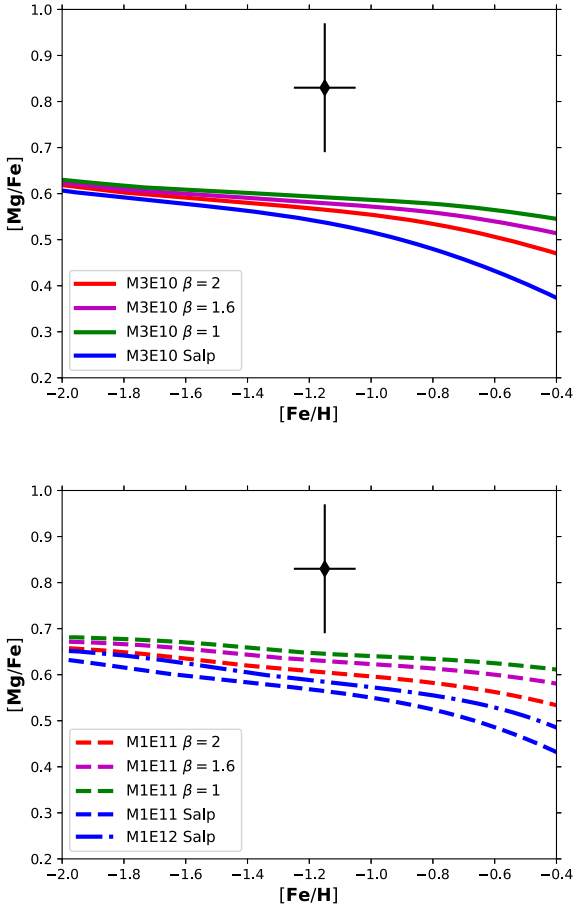

Figure 9. [Mg/Fe] versus [Fe/H] without accounting for dust depletion compared with abundances measured in galaxies of the sample of Table 3. Upper panel: lines are computed for M3E10 models (solid) with Salpeter (1955) IMF (blue) and W11 IGIMF calculated for $\beta = 1$ (green), $\beta = 1.6$ (magenta) and $\beta = 2$ (red). Lower panel: lines are computed for M1E11 models (dashed) with Salpeter (1955) IMF (blue), W11 IGIMF calculated for $\beta = 1$ (green), $\beta = 1.6$ (magenta), and $\beta = 2$ (red); M1E12 model with Salpeter (1955) (blue dash-dotted). For both panels: data are from Pettini et al. (2002) (diamond).

A sharp disagreement between model results and data is visible also in the [Mg/Fe]-[Fe/H] plots (Fig. 9).

The observed [O/Fe] values are higher than the ones of the M3E10 models, however the results obtained with the IGIMF and $\beta \leq 1.6$ lie within the observational errors (Fig. 10, top panel).

The abundances of all M1E11 models are in agreement with the observed [O/Fe] values, whereas the Salpeter IMF produces [O/Fe] values lower than the observed ones, and also outside of the error bars. Even if the Salpeter M1E12 model produces slightly overenhanced abundance ratios with respect to the M1E11 one, these are still inconsistent with the data. In summary, as for the [α/Fe]-[Fe/H] diagrams, the Si and Mg abundances computed with any of our models without taking into account dust production are lower than the ones observed in high-redshift lensed galaxies, whereas the O abundances derived with the models which include the IGIMF are in rather good agreement with the data.

In Figs 11–13 we show the results of our models computed taking into account the effects of dust depletion for the (C/O)-(O/H), [Si/Fe]-[Fe/H], and [O/Fe]-[Fe/H] diagrams, respectively, compared to the observational abundances derived in high-z galaxies described in Section 3 . In each figure, the top and bottom rows show the results of the M3E10 and M1E11 model, respectively. Such models trace separately the abundances in the gas and dust phases. It should also be noted that this is the first time in which the effects of dust are studied in chemical evolution models adopting an IGIMF.

We do not show our results including dust for the [Mg/Fe]-[Fe/H] diagram, because for Mg the observed abundances are available only for one system, and also because the theoretical abundances show a behaviour very similar to the one of [Si/Fe]-[Fe/H].

In Figs 11–13 the effects of dust depletion increase as one moves from left to right. In each figure, the leftmost plot shows the results of our 'minimal dust' models, which take into account dust destruction and the reverse shock in SNe dust yields, and which is therefore dubbed DR, with all the other processes switched off. The middle plot shows results for models in which dust depletion has intermediate effects and which includes dust condensation, destruction, and no reverse shock (ADNR). The rightmost plot

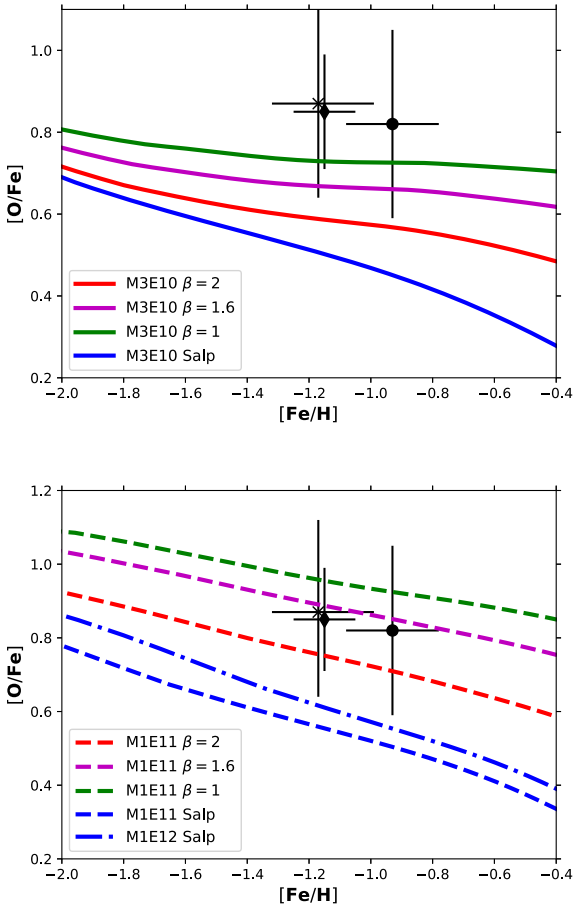

Figure 10. [O/Fe] versus [Fe/H] without accounting for dust depletion compared with abundances measured in galaxies of the sample of Table 3. Upper panel: lines are computed for M3E10 models (solid) with Salpeter (1955) IMF (blue) and W11 IGIMF calculated for $\beta = 1$ (green), $\beta = 1.6$ (magenta) and $\beta = 2$ (red). Lower panel: lines are computed for M1E11 models (dashed) with Salpeter (1955) IMF (blue), W11 IGIMF calculated for $\beta = 1$ (green), $\beta = 1.6$ (magenta) and $\beta = 2$ (red); M1E12 model with Salpeter (1955) (blue dash-dotted). For both panels: data are from Pettini et al. (2002) (diamond); Quider et al. (2009) (cross); Dessauges-Zavadsky et al. (2010) (filled circle).

shows results for our 'maximal dust' models, which includes only dust production from stars with no reverse shock in SNe (NR).

We have tested also a few additional models, not shown in this paper because they show a behaviour similar to the models of Figs 11–13. One model includes dust production in stars with reverse shock in SNe (R) and another has growth, destruction and reverse shock (ADR), in both of which the different prescriptions have small effects in the comparison with data points, relative to the DR model. On the other hand, another case in which dust depletion has intermediate effects is the model with destruction but no reverse shock (DNR), which produces results similar to the ADNR model.

In Fig. 11, the minimal dust DR models show small yet appreciable differences with respect to the ones of Fig. 7. An evident consequence of including dust depletion is to decrease the (C/O) ratio, as C is refractory and O is not. For this reason, the (C/O) values of the DR models of Fig. 11 are maximum by ∼0.1 lower than the ones of Fig. 7, with a small dependence on metallicity, i.e. with increasing depletion effects at larger values of 12+log(O/H).

The ADNR and NR models show larger C depletion effects and lower (C/O) values. The ADNR M3E10 models fall below the dark grey confidence region defined by the range of abundance values from the composite LBG spectra (Shapley et al. 2003), but are still consistent with the values measured in the lensed galaxies SGAS J105039.6+001730 and SMACS J2031.8-4036 (Bayliss et al. 2014; Christensen et al. 2012a,b). As for the M1E11 models, the abundances obtained in most of the ADNR models are by 0.1–0.15 dex lower than the DR models, all still consistent with the composite spectra confidence region. The results for the NR models are globally similar to the ones obtained in the case of the ADNR models.

As for the M3E10 model, the [Si/Fe]-[Fe/H] plots of Fig. 12 show that all the minimal dust models still underestimate the observed abundances. The models with the IGIMF show higher [Si/Fe] ratios, with distance from the data decreasing with decreasing β values, indicating that the abundance pattern of lensed high-z systems might show some signatures of a top-heavy IMF.

However, it is plausible that in such systems the effects of dust are important. If this is the case, they are clearly underestimated by our DR models.

All the ADNR models account satisfactorily for the observed abundances, in particular the Salpeter and the $\beta = 2$ model. All the NR models in which the IGIMF is adopted overestimate the observed abundances, although the abundances of the $\beta = 2$ model are within the $1 - \sigma$ error bars of two systems.

Similar suggestions come from the analysis of the M1E11 model results. ADNR and DR models show more enhanced [Si/Fe] ratios but still support a Salpeter-like IMF, or suggest that an IGIMF with $\beta < 2$ in the observed systems is to be excluded.

Also in the [O/Fe]-[Fe/H] diagram (Fig. 13), all the minimal dust M3E10 models underestimate the observed abundances. Even if all the IGIMF models systematically underproduce the observations, the $\beta < 2$ IGIMF models yield abundance values within the error bars. On the other hand, all the M1E11 IGIMF models show abundance ratios consistent with the observations. In both cases, the models with the Salpeter IMF underestimate the observed abundance pattern.

In all the other models where the effects of dust are more significant, the analysis of the M3E10 models support a Salpeter IMF or a moderate top-heavy (IGIMF with $\beta < 2$) in high-redshift galaxies, whereas all the M1E11 models with dust exclude the IGIMF.

4.4 Discussion

Previous chemical evolution studies including dust (Pipino et al. 2011) failed in reproducing the abundances of cB58 adopting a Salpeter (1955) IMF, but they did not considered differential depletion, i.e. different elements depleted in dust in different proportions. In this work instead, the use of elemental dust yields dependent on mass and metallicity of the stars allows us to account for differential dust depletion. If one focuses on a single mass model (M3E10 or ME11), our study shows that the effects of dust may produce variations in the abundance ratios larger than the ones driven by a different IMF.

If the effects of dust are marginal in our sample of high-redshift star-forming galaxies, our IGIMF models account for the observed abundance pattern better than the ones with a Salpeter IMF. On the other hand, if the effects of dust are moderate or high, the models with a Salpeter IMF or with the IGIMF with $\beta = 2$ allows

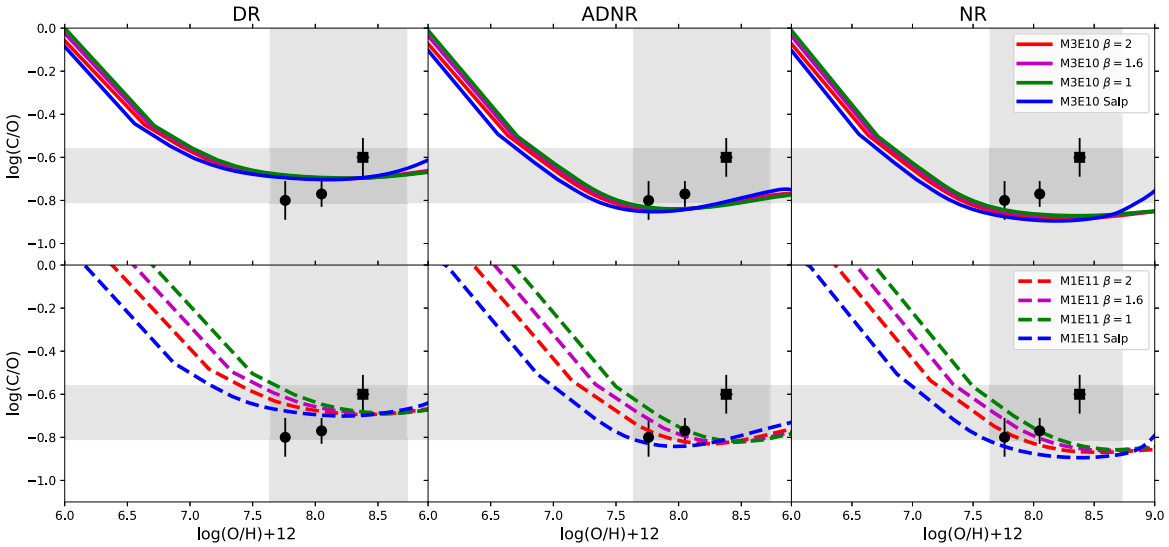

Figure 11. Same of Fig. 7, but with models considering dust.

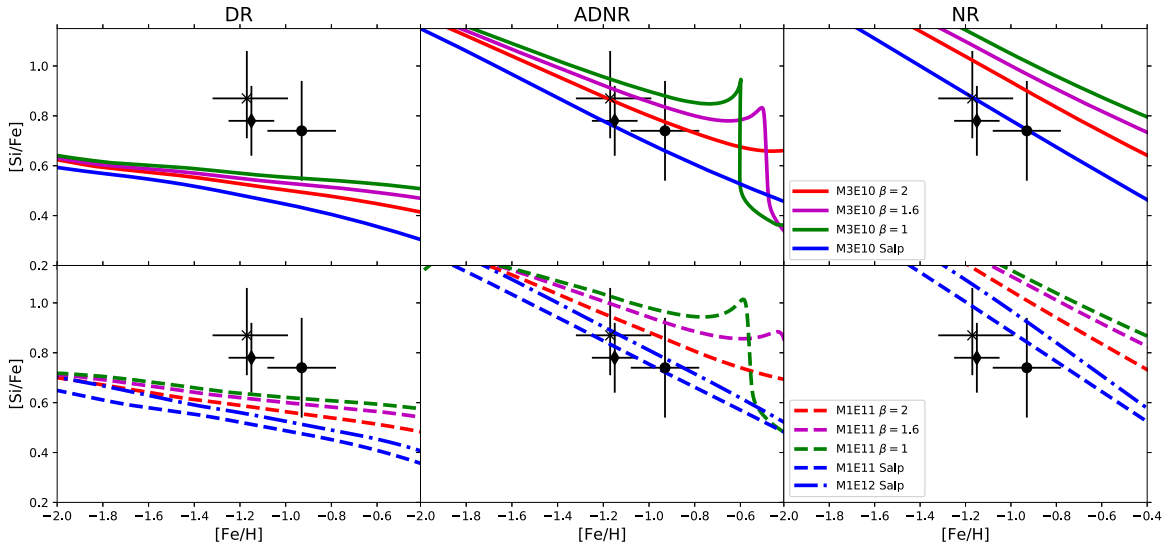

Figure 12. Same of Fig. 8, but with models considering dust.

us to reproduce the data, whereas the ones with more extreme assumptions for the IGIMF (i.e. $\beta \leq 1.6$) do not.

Our study is the first in which an extended data base of measured abundances from different chemical elements in lensed galaxies is compared with results from chemical evolution models. More observations are certainly needed in the future to shed more light on how the combined effects of dust depletion and IMF determine the abundance pattern of high-redshift galaxies.

In Fig. 14 we show the time evolution of the dust mass for our models with a Salpeter IMF and with an IGIMF, all computed adopting dust prescriptions as in the ADNR model (i. e. the model with intermediate dust depletion effects in Figs 11–13). Fig. 14 is useful to assess the time-scale for the buildup of dust and what is the role of the IMF in this process. In all models, a progressively steeper increase of the dust mass as a function of time is found as the value of β decreases. This highlights directly not only that a more top-heavy IMF produces a larger dust content, but also a faster buildup. As discussed in previous works (Gall, Hjorth & Andersen 2011; Mattsson 2011, 2015; Gioannini et al. 2017), a fast growth of dust goes in lockstep with a rapid buildup of refractory elements, clearly strongly dependent on the SFH. In starburst galaxies the buildup of the metals occurs on a particularly rapid time-scale, with a supersolar metallicity reached already at ∼0.1 Gyr (e.g. Calura et al. 2014).

In the case of a Salpeter IMF, in the M1E11 and M1E12 models the bulk of dust mass is already present at ∼0.25 Gyr after the beginning of star formation. Clearly, the rapid buildup of the dust also depends on the infall time-scale, which is shorter in larger systems. With these particular prescriptions for dust, the dust mass values attained with a Salpeter IMF after a few 0.1 Gyr are generally between $\sim 10^7$ and $\sim 10^8$ $M_\odot$, lower than the values observed in a large fraction of galaxies in the Herschel sample at comparable redshift, which in many cases show larger $> 10^8$ $M_\odot$ (Calura et al. 2017, Pozzi et al. 2020).

The same is not true for all the models with an IGIMF, which present dust mass values in excess of 10^8 $M_\odot$. This is particularly

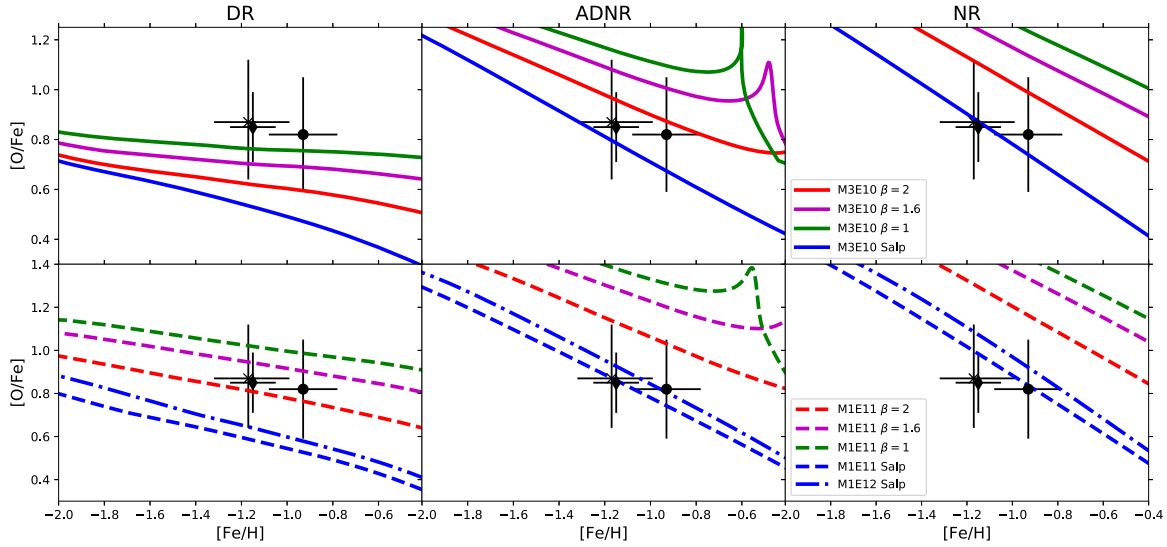

Figure 13. Same of Fig. 10, but with models considering dust.

evident for models with $\beta = 1$, which reach such values already after 0.2 Gyr.

This latter result is apparently in contrast with what is found from abundance patterns. However, uncertainties in the abundance data and in the elemental dust yields (e.g. Gall & Hjorth 2018 and references therein) have to be considered. Furthermore, in general, models with a moderate top-heavy IGIMF (i.e. $\beta = 2$) reasonably satisfy both the abundance and dust mass constraints.

The necessity to adopt a top-heavy IMF to solve the 'dust-budget crisis' (Rowlands et al. 2014) was already discussed by other authors (Gall et al. 2011; Mattsson 2011; Valiante et al. 2014 and references therein). However, this aspect was never highlighted before in the context of the IGIMF. Another important aspect of our study is that the interplay between varius parameters, including the IMF, in determining the abundance pattern in high-redshift galaxies and how these parameters influence the growth of the dust mass. At present, infrared-based determinations of the dust mass in Lyman-Break galaxies or in the sample considered in this work is lacking, but it will be valuable in the future to better single out the role of such parameters in determining the properties of high-redshift starbursts.

5 CONCLUSIONS

In this work, we have studied the effects of the integrated galactic IMF (as defined in W11) as well as interstellar dust evolution on the chemical evolution of high redshift starburst galaxies.

The IGIMF has a strong impact on the star formation history and chemical evolution of galaxies. In the IGIMF theory, in a galaxy the maximum mass of a stellar cluster increases with the SFR. In general, the higher is the SFR value, the larger is the fraction of massive stars (and the flatter is the IGIMF).

This affects several basic properties of galaxies, such as mass return from stellar populations, supernova rates, and even the star formation history; we have shown how the adoption of an IGIMF produces remarkable differences in these properties with respect to a classical Salpeter (1955) IMF.

Within the IGIMF theory, one key, yet unkown parameter which regulates the number of massive stars is the slope β of the embedded cluster mass function; in this work, we have tested three different values for this quantity.

In principle, the stellar populations of systems characterized by an intense star formation activity and by strong SFR values might present an overabundance of massive stars, whose signature might be present in the interstellar abundance pattern.

In order to probe the IMF of starburst galaxies, we have compared the abundance patterns computed by our models with the abundances observed in spectra of high redshift starburst galaxies, mainly LBGs and Lyman α emitters.

In our models, we have also taken into account the effects of dust depletion, which can have a strong impact on interstellar abundances, and which is fundamental to interpret the observed abundance pattern.

Our results can be summarized as follows.

(i) In all our models, the adoption of the IGIMF causes the increase of the rate of star formation with respect to the Salpeter IMF. In particular, the highest SFRs are obtained with the lowest values for the slope of the embedded cluster mass function β. This is a consequence of the behaviour of the IGIMF: the lower is β, the more top-heavy is the IMF. A high percentage of massive stars as due to a top-heavy IMF cause large quantities of gas to be restored into the ISM with CC-SN explosions, which in turn favour higher star formation rate values (as SFR $\propto M_{gas}$). On the other hand, we find a longer duration of the star formation phase for lower β values ($\beta = 1$ in particular), due to later galactic winds which, in our picture, cause the end of star formation.
In general, the higher the β value, the smaller the differences in the models with respect to the Salpeter IMF. In the models with $\beta = 2$, the occurrence of the galactic wind is comparable to the one obtained with a Salpeter IMF.
For the most extreme assumptions of the β value ($\beta = 1$), we have found a reduced Type Ia SN rate with respect to the Salpeter in M1E11 and M1E12 models. Moreover, we have found that with $\beta = 1$ the downsizing in star formation, i.e. winds occurring at earlier times in more massive galaxies, is not reproduced in the M3E10 and M1E11 models, despite a higher star formation efficiency for the larger mass model is adopted.

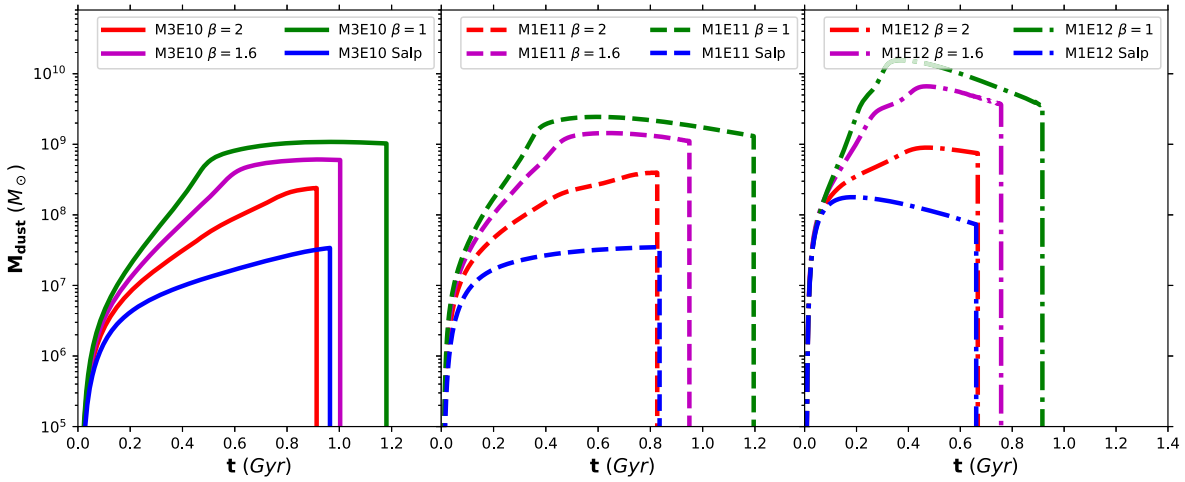

Figure 14. Dust mass as a function of time for our models computed with a Salpeter (1955) IMF (blue lines) and with W11 IGIMF with $\beta = 1$ (green lines), $\beta = 1.6$ (magenta lines) and $\beta = 2$ (red lines). In the left, middle, and right-hand panel we show our results computed for the M3E10 (solid lines), M1E11 (dashed lines), and M1E12 (dash-dotted lines) models, respectively.

(ii) The different star formation histories obtained with different IMFs have an impact on the evolution of chemical abundances. For a given galaxy mass, the more top-heavy the IMF (i.e. the lower the value for β), the faster is the growth of the metal content. As for the [α/Fe]-[Fe/H] diagram, in general, the lower the β, the higher the overabundance of α-elements, and the higher the metallicity at which the [α/Fe] starts to deviate from the initial plateau.
Our study also highlights the interplay between the IMF and the star formation efficiency in defining the interstellar abundance pattern. In particular, when the IGIMF is adopted, the lowest mass model can be characterized by values for the α-enhancement larger than what obtained with the Salpeter IMF in the most massive galaxy, in which a much larger star formation efficiency is adopted.

(iii) We have collected a data set of chemical abundances measured in high-redshift, star-forming galaxies. The sample consists of high-quality abundances for several elements (C, N, O, Mg, Si, Fe) as measured in lensed galaxies at $2 \lesssim z \lesssim 3$ and two `composite' spectra from sizable sets of high-z systems, obtained by means of observations in non-lensed fields. The observational results have been compared with our model results.
Some of the measured abundance ratios between volatile elements (O, N) are in agreement with our results in which the IGIMF is adopted, in particular in the (N/O) versus (O/H) plots. However, a large scatter in the data and large uncertainties in the stellar yields, in particular regarding N production, makes difficult the interpretation of the abundance ratios and the degeneracy between the effects of the IMF and the ones of stellar nucleosynthesis prevents us from reaching any firm conclusion.

(iv) To interpret the abundances for refractory elements, we have used models which can account for differential dust depletion (i.e. different elements depleted into dust in different proportions), and we have tested various assumptions regarding the processes that regulate the evolution of dust grains. All the models with minimal dust production (i.e. where dust destruction and the reverse shock in SNe are considered, whereas dust growth is not) underestimate the observed pattern in the [Si/Fe]-[Fe/H], [Mg/Fe]-[Fe/H] and [O/Fe]-[Fe/H] diagrams. Under these conditions, the models with the IGIMF give [α/Fe] values in better agreement with the observations with respect to the ones with a Salpeter IMF.
On the other hand, if the effects of dust are important, our analysis suggest a Salpeter or an IGIMF with $\beta \geq 2$, i.e. slightly more top heavy than the Salpeter but not particularly extreme. Several previous studies have evidenced that high-redshift star-forming galaxies can contain large amounts of dust (e. g., Calura et al. 2017 and references therein, Gall & Hjorth 2018). In the light of this, a scenario in which the effects of dust are negligible seems not plausible.
We have also calculated the evolution of the dust mass with time for galaxies of different stellar mass and IMF, showing that an at least moderate top-heavy IGIMF is required to solve the 'dust budget crisis' problem (e.g. Valiante et al. 2014).

Other works support a top-heavy IMF in high-redshift starbursts, in particular a few studies based on the interpretation by means of chemical evolution models of the abundances of rare isotopes such as ^{13}C, ^{15}N, ^{17}O, and ^{18}O ratios, detected in the infrared band (Romano et al. 2017; Zhang et al. 2018). In the future, it will be important to take into account the IGIMF in models to interpret such measures, and possibly assess better the role of downsizing in the star formation histories of such systems.

On the observational side, the Multi Unit Spectroscopic Explorer (MUSE) mounted on the VLT has allowed the identification and the spectroscopic confirmation of hundreds of multiple images in the redshift range $2 \leq z \lesssim 7$ (e. g., Vanzella et al. 2017 and references therein).

This has also enabled the production of highly accurate lens models, useful to determine and interpret absolute physical quantities such as luminosities, stellar masses, star formation rate values and abundances of high-redshift galaxies (e. g., Meneghetti et al. 2017). In the future, it will be important to perform high-resolution spectroscopic follow-ups of the most magnified sources, in order to derive precise abundance ratios and to extend the observational sample presented in this work.

ACKNOWLEDGEMENTS

MP, FM acknowledge financial support from the University of Trieste (FRA2016). FC acknowledges the support from grant PRIN MIUR 2017–20173ML3WW_001 and the INAF main-stream (1.05.01.86.31). FV acknowledges the support of a Fellowship from

the Center for Cosmology and AstroParticle Physics at The Ohio State University. The authors thank the anonymous referee for careful reading of the manuscript and useful suggestions.

REFERENCES

Allam S. S., Lin H., Tucker D., Buckley-Geer E., Kubik D., Diehl T., Annis J., Frieman J., 2007, in American Astronomical Society Meeting Abstracts. p. 99.02

Asano R. S., Takeuchi T. T., Hirashita H., Inoue A. K., 2013, Earth Planets Space, 65, 213

Asplund M., Grevesse N., Sauval A. J., Scott P., 2009, ARA&A, 47, 481

Baker A. J., Tacconi L. J., Genzel R., Lehnert M. D., Lutz D., 2004, ApJ, 604, 125

Bastian N., 2008, MNRAS, 390, 759

Baugh C. M., Lacey C. G., Frenk C. S., Granato G. L., Silva L., Bressan A., Benson A. J., Cole S., 2005, MNRAS, 356, 1191

Bayliss M. B., Rigby J. R., Sharon K., Wuyts E., Florian M., Gladders M. D., Johnson T., Oguri M., 2014, ApJ, 790, 144

Belokurov V. et al., 2007, ApJ, 671, L9

Bianchi S., Schneider R., 2007, MNRAS, 378, 973

Bradamante F., Matteucci F., D'Ercole A., 1998, A&A, 337, 338

Calura F., Matteucci F., 2006, ApJ, 652, 889

Calura F., Menci N., 2009, MNRAS, 400, 1347

Calura F., Pipino A., Matteucci F., 2008, A&A, 479, 669

Calura F., Recchi S., Matteucci F., Kroupa P., 2010, MNRAS, 406, 1985

Calura F., Gilli R., Vignali C., Pozzi F., Pipino A., Matteucci F., 2014, MNRAS, 438, 2765

Calura F. et al., 2017, MNRAS, 465, 54

Cenarro A. J., Gorgas J., Vazdekis A., Cardiel N., Peletier R. F., 2003, MNRAS, 339, L12

Chiappini C., Romano D., Matteucci F., 2003, MNRAS, 339, 63

Christensen L. et al., 2012a, MNRAS, 427, 1953

Christensen L. et al., 2012b, MNRAS, 427, 1973

Conroy C., van Dokkum P., 2012a, ApJ, 747, 69

Conroy C., van Dokkum P. G., 2012b, ApJ, 760, 71

Davé R., 2008, MNRAS, 385, 147

De Masi C., Matteucci F., Vincenzo F., 2018, MNRAS, 474, 5259

Dell'Agli F., García-Hernández D. A., Schneider R., Ventura P., La Franca F., Valiante R., Marini E., Di Criscienzo M., 2017, MNRAS, 467, 4431

Dessauges-Zavadsky M., D'Odorico S., Schaerer D., Modigliani A., Tapken C., Vernet J., 2010, A&A, 510, A26

Dwek E., 1998, ApJ, 501, 643

Dye S., Evans N. W., Belokurov V., Warren S. J., Hewett P., 2008, MNRAS, 388, 384

Ferrara A., Viti S., Ceccarelli C., 2016, MNRAS, 463, L112

Ferreras I., Weidner C., Vazdekis A., La Barbera F., 2015, MNRAS, 448, L82

Finkelstein S. L., Papovich C., Rudnick G., Egami E., Le Floc'h E., Rieke M. J., Rigby J. R., Willmer C. N. A., 2009, ApJ, 700, 376

François P., Matteucci F., Cayrel R., Spite M., Spite F., Chiappini C., 2004, A&A, 421, 613

Gall C., Hjorth J., 2018, ApJ, 868, 62

Gall C., Hjorth J., Andersen A. C., 2011, A&A Rev., 19, 43

Garnett D. R., Skillman E. D., Dufour R. J., Peimbert M., Torres-Peimbert S., Terlevich R., Terlevich E., Shields G. A., 1995, ApJ, 443, 64

Gibson B. K., Matteucci F., 1997, MNRAS, 291, L8

Gioannini L., Matteucci F., Vladilo G., Calura F., 2017, MNRAS, 464, 985

Gomez H. L. et al., 2012, ApJ, 760, 96

Grieco V., Matteucci F., Calura F., Boissier S., Longo F., D'Elia V., 2014, MNRAS, 444, 1054

Hainline K. N., Shapley A. E., Kornei K. A., Pettini M., Buckley-Geer E., Allam S. S., Tucker D. L., 2009, ApJ, 701, 52

Israelian G., Ecuvillon A., Rebolo R., García-López R., Bonifacio P., Molaro P., 2004, A&A, 421, 649

Iwamoto K., Brachwitz F., Nomoto K., Kishimoto N., Umeda H., Hix W. R., Thielemann F.-K., 1999, ApJS, 125, 439

Jeřábková T., Kroupa P., Dabringhausen J., Hilker M., Bekki K., 2017, A&A, 608, A53

Jeřábková T., Hasani Zonoozi A., Kroupa P., Beccari G., Yan Z., Vazdekis A., Zhang Z. Y., 2018, A&A, 620, A39

Kennicutt R. C. Jr, 1998, ApJ, 498, 541

Kroupa P., 2001, MNRAS, 322, 231

Kroupa P., 2002, Science, 295, 82

Kroupa P., Weidner C., 2003, ApJ, 598, 1076

La Barbera F., Ferreras I., Vazdekis A., de la Rosa I. G., de Carvalho R. R., Trevisan M., Falcón-Barroso J., Ricciardelli E., 2013, MNRAS, 433, 3017

Lacchin E., Matteucci F., Vincenzo F., Palla M., 2019, preprint (arXiv: 1911.08450)

Lada C. J., Lada E. A., 2003, ARA&A, 41, 57

Larson R. B., 1998, MNRAS, 301, 569

Lüghausen F., Famaey B., Kroupa P., Angus G., Combes F., Gentile G., Tiret O., Zhao H., 2013, MNRAS, 432, 2846

Lüghausen F., Famaey B., Kroupa P., 2015, Can. J. Phys., 93, 232

Massey P., Hunter D. A., 1998, ApJ, 493, 180

Matteucci F., 1986, MNRAS, 221, 911

Matteucci F., 1994, A&A, 288, 57

Matteucci F., 2012, Chemical Evolution of Galaxies. Springer, Berlin

Matteucci F., Greggio L., 1986, A&A, 154, 279

Matteucci F., Pipino A., 2002, ApJ, 569, L69

Matteucci F., Recchi S., 2001, ApJ, 558, 351

Mattsson L., 2011, MNRAS, 414, 781

Mattsson L., 2015, preprint (arXiv:1505.04758)

Megeath S. T. et al., 2016, AJ, 151, 5

Meneghetti M. et al., 2017, MNRAS, 472, 3177

Meynet G., Maeder A., 2002, A&A, 390, 561

Nittler L. R., O'D. Alexander C. M., Liu N., Wang J., 2018, ApJ, 856, L24

Nozawa T., Maeda K., Kozasa T., Tanaka M., Nomoto K., Umeda H., 2011, ApJ, 736, 45

Palla M., Matteucci F., Calura F., Longo F., 2020, ApJ, 889, 4

Pettini M., Steidel C. C., Adelberger K. L., Dickinson M., Giavalisco M., 2000, ApJ, 528, 96

Pettini M., Shapley A. E., Steidel C. C., Cuby J.-G., Dickinson M., Moorwood A. F. M., Adelberger K. L., Giavalisco M., 2001, ApJ, 554, 981

Pettini M., Rix S. A., Steidel C. C., Adelberger K. L., Hunt M. P., Shapley A. E., 2002, ApJ, 569, 742

Pflamm-Altenburg J., Weidner C., Kroupa P., 2007, ApJ, 671, 1550

Pipino A., Matteucci F., 2004, MNRAS, 347, 968

Pipino A., Matteucci F., 2011, A&A, 530, A98

Pipino A., Matteucci F., Borgani S., Biviano A., 2002, New Astron., 7, 227

Pipino A., Fan X. L., Matteucci F., Calura F., Silva L., Granato G., Maiolino R., 2011, A&A, 525, A61

Pozzi F., Calura F., Zamorani G., Delvecchio I., Gruppioni C., Santini P., 2020, MNRAS, 491, 5073

Quider A. M., Pettini M., Shapley A. E., Steidel C. C., 2009, MNRAS, 398, 1263

Recchi S., Matteucci F., D'Ercole A., 2001, MNRAS, 322, 800

Recchi S., Calura F., Kroupa P., 2009, A&A, 499, 711

Recchi S., Calura F., Gibson B. K., Kroupa P., 2014, MNRAS, 437, 994

Rigby J. R., Wuyts E., Gladders M. D., Sharon K., Becker G. D., 2011, ApJ, 732, 59

Romano D., Karakas A. I., Tosi M., Matteucci F., 2010, A&A, 522, A32

Romano D., Matteucci F., Zhang Z. Y., Papadopoulos P. P., Ivison R. J., 2017, MNRAS, 470, 401

Rowlands K., Gomez H. L., Dunne L., Aragón-Salamanca A., Dye S., Maddox S., da Cunha E., van der Werf P., 2014, MNRAS, 441, 1040

Salpeter E. E., 1955, ApJ, 121, 161

Salvador-Rusiñol N., Vazdekis A., La Barbera F., Beasley M. A., Ferreras I., Negri A., Dalla Vecchia C., 2019, Nature Astronomy, 4, 252

Schmidt M., 1959, ApJ, 129, 243

Seitz S., Saglia R. P., Bender R., Hopp U., Belloni P., Ziegler B., 1998, MNRAS, 298, 945
Shapley A. E., Steidel C. C., Pettini M., Adelberger K. L., 2003, ApJ, 588, 65
Siana B., Teplitz H. I., Chary R.-R., Colbert J., Frayer D. T., 2008, ApJ, 689, 59
Spite M. et al., 2005, A&A, 430, 655
Spolaor M., Kobayashi C., Forbes D. A., Couch W. J., Hau G. K. T., 2010, MNRAS, 408, 272
Steidel C. C. et al., 2014, ApJ, 795, 165
Steidel C. C., Strom A. L., Pettini M., Rudie G. C., Reddy N. A., Trainor R. F., 2016, ApJ, 826, 159
Teplitz H. I. et al., 2000, ApJ, 533, L65
Thies I., Pflamm-Altenburg J., Kroupa P., Marks M., 2015, ApJ, 800, 72
Thomas D., Maraston C., Schawinski K., Sarzi M., Silk J., 2010, MNRAS, 404, 1775
Valiante R., Schneider R., Salvadori S., Gallerani S., 2014, MNRAS, 444, 2442
van den Hoek L. B., Groenewegen M. A. T., 1997, A&AS, 123, 305
Vanzella E. et al., 2017, MNRAS, 467, 4304
Vincenzo F., Kobayashi C., 2018, A&A, 610, L16
Vincenzo F., Matteucci F., Recchi S., Calura F., McWilliam A., Lanfranchi G. A., 2015, MNRAS, 449, 1327
Vincenzo F., Belfiore F., Maiolino R., Matteucci F., Ventura P., 2016, MNRAS, 458, 3466
Vladilo G., Gioannini L., Matteucci F., Palla M., 2018, ApJ, 868, 127
Weidner C., Kroupa P., 2004, MNRAS, 348, 187
Weidner C., Kroupa P., 2005, ApJ, 625, 754
Weidner C., Kroupa P., Larsen S. S., 2004, MNRAS, 350, 1503
Weidner C., Kroupa P., Pflamm-Altenburg J., 2011, MNRAS, 412, 979
Weidner C., Ferreras I., Vazdekis A., La Barbera F., 2013, MNRAS, 435, 2274
Woosley S. E., Weaver T. A., 1995, ApJS, 101, 181
Wuyts E. et al., 2010, ApJ, 724, 1182
Yan Z., Jerabkova T., Kroupa P., 2017, A&A, 607, A126
Yan Z., Jerabkova T., Kroupa P., Vazdekis A., 2019, A&A, 629, A93
Yee H. K. C., Ellingson E., Bechtold J., Carlberg R. G., Cuillandre J. C., 1996, AJ, 111, 1783
Zhang Z.-Y., Romano D., Ivison R. J., Papadopoulos P. P., Matteucci F., 2018, Nature, 558, 260

This paper has been typeset from a TEX/LATEX file prepared by the author.